

AD-A139 077

UPPER OCEAN SHEAR DURING JASIN: A DETERMINISTIC AND
STATISTICAL ANALYSIS(U). SCIENCE APPLICATIONS INC MCLEAN
VA D M RUBENSTEIN FEB 84 SAI-84-1027 N00014-83-C-0057

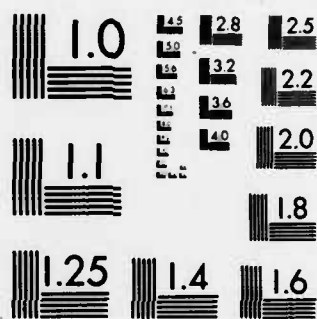
1//

UNCLASSIFIED

F/G 8/3

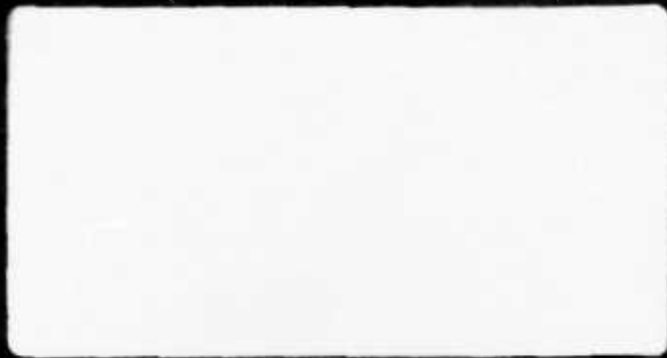
NL





MICROCOPY RESOLUTION TEST CHART
NATIONAL BUREAU OF STANDARDS-1963-A

AD A 139077



UPPER OCEAN SHEAR DURING JASIN:
A DETERMINISTIC AND STATISTICAL ANALYSIS

SAI-84/1027

DTIC
ELECTE
S MAR 19 1984 D
B



SCIENCE APPLICATIONS, INC.

Post Office Box 1303, 1710 Goodridge Drive, McLean, Virginia 22102, (703) 821-4300

DISTRIBUTION STATEMENT A

Approved for public release
Distribution Unlimited

UPPER OCEAN SHEAR DURING JASIN:
A DETERMINISTIC AND STATISTICAL ANALYSIS

SAI-84/1027

February 1984

Prepared by:
David M. Rubenstein

Prepared for:
Naval Ocean Research and Development Activity
Ocean Measurements Program, Code 541
NSTL Station, Mississippi 39529

Final Report for Contract No. N00014-83-C-0057

SCIENCE APPLICATIONS, INC.

1710 Goodridge Drive
P.O. Box 1303
McLean, Virginia 22102
(703) 821-4300



UNCLASSIFIED

SECURITY CLASSIFICATION OF THIS PAGE (When Data Entered)

REPORT DOCUMENTATION PAGE		READ INSTRUCTIONS BEFORE COMPLETING FORM
1. REPORT NUMBER SAI-84/1027	2. GOVT ACCESSION NO. AD-A2	3. RECIPIENT'S CATALOG NUMBER 39077
4. TITLE (and Subtitle) Upper Ocean Shear during JASIN: A Deterministic and Statistical Analysis		5. TYPE OF REPORT & PERIOD COVERED
7. AUTHOR(s) David M. Rubenstein		6. PERFORMING ORG. REPORT NUMBER SAI-84/1027
9. PERFORMING ORGANIZATION NAME AND ADDRESS Science Applications, Inc. 1710 Goodridge Drive P.O. Box 1303, McLean, VA 22102		8. CONTRACT OR GRANT NUMBER(s) N00014-83-C-0057
11. CONTROLLING OFFICE NAME AND ADDRESS NORDA, Code 540 Ocean Measurements Program NSTL Station, Bay St. Louis, MS 39529		10. PROGRAM ELEMENT, PROJECT, TASK AREA & WORK UNIT NUMBERS
14. MONITORING AGENCY NAME & ADDRESS (if different from Controlling Office) Same		12. REPORT DATE February, 1984
		13. NUMBER OF PAGES 76
		15. SECURITY CLASS. (of this report) Unclassified
		16. DECLASSIFICATION/DOWNGRADING SCHEDULE
18. DISTRIBUTION STATEMENT (of this Report) Distribution unlimited; approved for public release		
17. DISTRIBUTION STATEMENT (of the abstract entered in Block 20, if different from Report) Same		
19. SUPPLEMENTARY NOTES		
19. KEY WORDS (Continue on reverse side if necessary and identify by block number) Upper Ocean Shear Internal Waves Tides JASIN		
20. ABSTRACT (Continue on reverse side if necessary and identify by block number) See reverse side		

UNCLASSIFIED

SECURITY CLASSIFICATION OF THIS PAGE(When Data Entered)

ABSTRACT

The shear field measured by the W1 mooring during JASIN 1978 was analyzed, using deterministic and statistical approaches. A significant fraction of the shear variance was at the semidiurnal tidal frequency. In order to determine whether the shear was associated with internal wave trains propagating from single or multiple sources, the eccentricity of the shear ellipse was analyzed. During seven periods of intense shear, the minor-to-major axis ratio was consistent with the theoretically predicted ratio of 0.89 for coherent internal waves. From the orientation of the shear ellipse, the probable source of the internal tides during three of these intense periods was found to be the Rockall Bank.

A statistical model of shear was applied during two periods of the JASIN experiment. The mean-square velocity difference, $\overline{\Delta u^2} + \overline{\Delta v^2} = S^2 \Delta z^2$, was normalized in terms of $2N^2/k_0$. The normalized value, $k_0 S^2 \Delta z^2 / 2N^2$, was found to be proportional to Δz . Here, S is shear magnitude, N is Vaisala frequency, $k_0 = 0.1$ cpm is a fall-off wavenumber, and Δz is the vertical separation of the current measurements over which the velocity difference was calculated. Internal wave-induced shear during Period 2 was comparable in level to that measured during MILE, but levels recorded during Period 1 were 40% higher. This variability is attributed to changes in the propagation of the internal tide, associated with the evolving field of mesoscale eddies.

Accession For	
NTIS GRA&I	<input checked="checked" type="checkbox"/>
DTIC TAB	<input type="checkbox"/>
Unannounced	<input type="checkbox"/>
Justification	
By	
Distribution/	
Availability Codes	
Dist	Avail and/or Special
A-1	

UNCLASSIFIED

SECURITY CLASSIFICATION OF THIS PAGE(When Data Entered)

TABLE OF CONTENTS

<u>Section</u>	<u>Page</u>
LIST OF FIGURES	ii
1 INTRODUCTION	1-1
1.1 BACKGROUND	1-1
1.2 DETERMINISTIC APPROACH	1-3
1.3 STATISTICAL APPROACH	1-4
2 INSTRUMENTATION DEPLOYMENT AND DATA PROCESSING ...	2-1
2.1 CURRENT METERS	2-1
2.2 CTD SURVEYS AND VAISALA PROFILES	2-4
2.2.1 Salinity and Temperature Gradient Contributions to Vaisala Frequency ...	2-5
2.2.2 Average Vaisala Frequency Profiles ...	2-10
3 DETERMINISTIC DESCRIPTION OF CURRENT AND SHEAR ...	3-1
3.1 CURRENT FIELD	3-1
3.2 SHEAR FIELD	3-13
4 SHEAR STATISTICS	4-1
4.1 FILTERING PROCESS	4-1
4.2 $S^2 - N^2$ CORRELATIONS	4-1
4.3 ANALYSIS	4-9
5 CONCLUSIONS	5-1
APPENDIX A: COMPLEX DEMODULATION	A-1
APPENDIX B: STATISTICAL MODEL OF MEAN-SQUARE SHEAR	B-1
REFERENCES	R-1

LIST OF FIGURES

<u>Figure</u>	<u>Page</u>
2.1 The JASIN area in relation to the British Isles..	2-2
2.2 JASIN 1978 hydrographic survey area.....	2-3
2.3 CTD profile on August 7, at 02:35 GMT, taken from the <u>Tydemar</u>	2-6
2.4 Vaisala frequency profile, from CTD cast on August 7 at 02:35 GMT.....	2-9
2.5 Vaisala frequency N, for mean profiles in (a) period 1 and (b) period 2.....	2-11
2.6 Brunt-Vaisala frequency profiles, averaged over Period 1 (31 July to 9 August) and Period 2 (23 August to 6 September)	2-13
3.1 Current at 124 m depth from the JASIN W1 mooring mooring, projected onto four coordinate frames. Each frame is rotated by successive 45° angles CCW with respect to east.....	3-2
3.2 Dynamic heights (dynamic mm) at 200 dbar ad- justed to a level of no motion at the bottom. Light arrows show estimated geostrophic veloci- ties and heavy arrows show 200 m current obser- vations. (a) Survey B, 31 July to 11 August 1978. b) Survey C, 20-29 August 1978.....	3-5
3.3 Power spectral density of 79 m current.....	3-6
3.4 Power spectrum of 79 m current, in variance preserving form.....	3-8
3.5 Amplitudes of clockwise (solid) and counter- clockwise (dashed) rotary components of 79 m current, at the semidiurnal tidal frequency	3-9
3.6 Ratio of minor to major axes, for tidal ellipse described by 79 m current.....	3-11
3.7 Time series of u-component of velocity at four depths; 79, 124, 200, and 300 m.....	3-12

LIST OF FIGURES (Continued)

<u>Figure</u>		<u>Page</u>
3.8	Time series of u-component of velocity difference over depth intervals 91-94 m, 94-97 m, 97-100 m, and 100-103 m.....	3-14
3.9	Power spectral density of velocity difference across 79-124 m.....	3-16
3.10	Power spectrum of velocity difference across 79-124 m, in variance preserving form.....	3-17
3.11	Complex demodulation of 79-124 m velocity difference, at the semidiurnal frequency.....	3-18
3.12	Peak-to-peak envelope of semidiurnal temperature oscillations, at 79 m depth.....	3-18
3.13	Ratio of minor-to-major axes, for tidal ellipse described by 79-124 m velocity difference.....	3-22
3.14	Velocity difference across 79-124 m resolved into four components; 0°, 45°, 90° and 135° CCW from due east, and demodulated at the semidiurnal frequency.....	3-23
3.15	Schematic directions of internal tide packets during seven periods of intense baroclinic tide activity.....	3-26
4.1	Mean-square shear across 3 m intervals vs. mean-square Vaisala frequency, during Period 1 (31 July to 9 August) and Period 2 (23 August to 6 September)	4-3
4.2	Mean-square shear across 6 m intervals vs. mean-square Vaisala frequency, during Period 1 (31 July to 9 August) and Period 2 (23 August to 6 September)	4-4
4.3	Mean-square shear across 12 m intervals vs. mean-square Vaisala frequency, during Period 1 (31 July to 9 August) and Period 2 (23 August to 6 September)	4-5

LIST OF FIGURES (Continued)

<u>Figure</u>		<u>Page</u>
4.4	Mean-square shear across 15 m intervals vs. mean-square Vaisala frequency, during Period 1 (31 July to 9 August) and Period 2 (23 August to 6 September)	4-6
4.5	Mean-square shear across 24 m intervals vs. mean-square Vaisala frequency, during Period 1 (31 July to 9 August) and Period 2 (23 August to 6 September)	4-7
4.6	Mean square velocity difference vs vertical separation interval, Δz . The JASIN Period 1 data fit the model with $A=1$, and the JASIN Period 2 and MILE data are best with $A=0.7$	4-10
A.1	Amplitude of the frequency response function $\hat{w}_L(f)$. The amplitude is 0.5 at the cut-off frequency $f_c = 0.016$ cph	A-3
B.1	Idealized Shear Spectrum after Gargett <u>et al.</u> (1981) Roll-off Wavenumber $k_0 = 0.1$ cpm Buoyancy Wavenumber $k_D = 1$ cpm	B-3
B.2	Model prediction of mean-square velocity difference, from Equation (B.13). Parameter values are $k_0 = 0.1$ cpm, $k_D = 1$ cpm, and $A = 1$. The two dashed curves indicate the separate contributions due to I_1 and I_2 , and the solid curve is the sum total	B-6
B.3	Model prediction for mean-square velocity difference over vertical differencing interval Δz . The fall-off wavenumber values are $k_0 = 0.1$ cpm for the solid curve, and $k_0 = 0.2$ and 0.05 cpm for the upper and lower dashed curves, respectively.....	B-7

Section 1 INTRODUCTION

1.1 BACKGROUND

The ocean environment directly affects systems operating in it. The difficulties in quantifying ocean variability often prevent addressing important environmental issues during the design stages of these systems. Therefore, NORDA's Ocean Measurements Program (OMP) has been developing techniques to describe the upper ocean environment. SAI has been supporting this program since 1978. Particular emphasis has been paid to internal waves, vertical shear, fine structure, and turbulence. The motivation is that an understanding of these processes may lead to a capability for predicting ocean variability.

Much attention has been given in recent years to the measurement and description of vertical shear. A very important result of this work is that a significant component of shear is deterministic in character. Rubenstein and Newman (1982a) showed that in the upper ocean during MILE (Mixed Layer Experiment), much of the shear near the top of the thermocline is inertial. In other words, the low-frequency component of the shear vector often describes a nearly circular orbit: It rotates clockwise at nearly the inertial frequency $f = 2\Omega \sin \phi$, where Ω is the Earth's angular rotation rate and ϕ is the latitude.

Inertial motions are usually strongest in the upper ocean, where they are predominantly generated locally, in response to surface winds. Pollard and Millard (1969), and

later Kundu (1976) showed that a simple local wind-forced model was adequate to reproduce much of the variability of inertial currents in the surface layer. Weller (1982) and Weller and Halpern (1983) analyzed the upper ocean velocity field during JASIN (Joint Air-Sea Interaction Project). They found that the near-inertial currents were significantly coherent with the local wind stress. However, they found that the coherence between near-inertial shear and the wind stress was even greater. Therefore, it is often feasible to predict shear variability near the ocean surface, as a function of the local winds.

The strength of inertial motions decays rapidly with increasing depth below the surface layer. As a consequence, other deterministic-types of motions--most notably tides--gain in relative importance. In the vicinity of steeply sloped bathymetry, shear can exhibit a strong tidal component. For example, Regal and Wunsch (1973) described observations of internal tides at several ocean stations, including Site D, over the continental slope in the western North Atlantic. The barotropic semidiurnal tide interacts with the nearby continental shelf, and generates internal tides at locations where sharp changes in the bottom slope occur. Internal waves at the tidal frequency then propagate along characteristic lines. At Site D internal tidal energy seems to be focused near the surface after a single bottom bounce. Rubenstein and Newman (1982b) analyzed the shear from an array of three current meter moorings near Site D. For the most part, the inertial component of shear was dominant, but in one case (between 12 and 32 m), shear at the semidiurnal tidal frequency was comparable to the inertial component.

Unfortunately, deterministic models of near-inertial shear are not yet reliable. The reason is that the mechanisms of generation and propagation of inertial and tidal internal waves are not sufficiently understood. Therefore, supplementary statistical treatments must be used for estimates of shear magnitude. In the ocean's main thermocline, statistics are obtained through spatial averages of shear profiles. In the seasonal thermocline, where background stratification and shear are strongly depth-dependent, spatial averages are inappropriate. However, the long-term deployment of current meters allows a time-averaging approach for measuring shear statistics.

The goal of the present study is to improve our capability for predicting upper-ocean shear variability in the near-inertial frequency range. Shear data from the JASIN experiment are analyzed from two complementary approaches. In the deterministic approach we analyze the time-dependence and directionality of the dominant semidiurnal tide component of shear. In the statistical approach we analyze the relationship between shear variance, and background stratification and vertical scale.

1.2 DETERMINISTIC APPROACH

In the present study, shear data from the JASIN experiment are analyzed. The W1 mooring collected data continuously over a 39-day period. Current meters were deployed across the depth range from 79 to 124 m at 3 m intervals. Therefore, shear--computed by taking the difference between currents measured by a pair of vertically-separated current meters--is obtained over vertical intervals ranging from 3 to 45 m.

The major steps in the deterministic approach are as follows. The first step is to establish by spectral analysis of the shear that, indeed, the semidiurnal frequency component of shear is dominant. Then, a process called complex demodulation is used to extract the time-dependent amplitude of the semidiurnal shear. We observe the time periods of variability of semidiurnal shear, and then make a qualitative comparison between its amplitude and the amplitude of the internal tide (as seen in a temperature record).

Then we show that the shear vector associated with a single coherent train of internal waves follows an elliptical orbit. The orbit's eccentricity can be related to the frequency of the wave, and the direction of orientation of the major axis is parallel to the horizontal direction of wave propagation. Therefore, we analyze the orientation of the orbit of the semidiurnal shear vector. This analysis gives us some indication of the direction of propagation of the internal tide. Therefore, we get some clues as to which of the nearby bathymetric features are interacting with the barotropic tide, and helping to produce the baroclinic internal tide.

1.3 STATISTICAL APPROACH

A quantification of the vertical length scales of shear is important to the design and deployment of submerged systems (moored, unmoored, and towed arrays, submarines, pipelines, oil rigs, etc.). Vertical profiles of shear display a broad range of length scales. However, it is difficult to quantify the length scales of shear in the upper seasonal thermocline. A vertically profiling instrument

passes but once through any given depth. The length scales of shear vary significantly with depth, due to the rapidly varying background stratification. Therefore, WKB scaling of shear is not appropriate. For these reasons, a single vertical profile is not sufficient to generate an ensemble of statistically independent measurements of shear (in a particular stratification regime) in the upper thermocline.

In principle, it might be possible to overcome this problem by performing a series of instrument casts. Adjacent casts would have to be separated temporally by the decorrelation time--at least three hours. A number of casts would be necessary, so that the time span of the experiment could conceivably be several days to a week. Such an experimental program is quite likely to be impractical aboard a non-dedicated vessel.

An obvious solution is the use of moored current meters. Current meters need not be attended for weeks or months at a time. They lend themselves to extended-duration observational programs, during which large ensembles of statistically independent shear measurements can be collected. A disadvantage to this solution is that shear can only be measured at discrete depths, across discrete vertical intervals. This disadvantage is mitigated somewhat by the recent deployment of large, closely spaced arrays of current meters (for example, during MILE and JASIN).

In the present work, we take an approach very similar to that used by Rubenstein, Newman, and Grabowski (1983). We use a statistical model of shear variance based upon an idealized version of the vertical wavenumber spectrum

proposed by Gargett et al. (1981). This idealized spectrum was based on a composite of spectra from a series of vertical profiles in the Sargasso Sea. The spectra were evaluated over depths ranging between 200 and 1500 m. In this depth range, the Vaisala frequency varied slowly, and WKB scaling was justified.

The statistical model provides a framework for quantifying the vertical length scales of shear from current meter time series. It converts the profile-based idealized spectrum into a form directly applicable to time-series measurements from current meters. The model predicts a relationship between shear (or velocity difference) variance and the vertical interval across which the shear is measured.

We compute time averages of mean-square velocity difference from the JASIN W1 mooring, over a range of vertical separations and Vaisala frequencies. The results are compared against similar measurements from MILE, and against the model predictions.

Section 2

INSTRUMENTATION DEPLOYMENT AND DATA PROCESSING

The primary aims of JASIN were to examine the mixing processes, momentum and heat budgets, and fluxes across and between the atmospheric and oceanic boundary layers. The JASIN experiment took place from July to September 1978 in the North Rockall Trough (see Figure 2.1). This is a deep water area, several hundred kilometers off the west coast of Scotland. It was a large project--14 ships, 3 aircraft, and 35 mooring systems were deployed by many investigators from nine countries.

Two of the instrument systems are especially relevant to this study; the W1 current meter mooring, and the conductivity-temperature-depth (CTD) probe deployed by the Dutch oceanographic vessel Tydeman. The purpose of this section is to discuss the deployment and data processing performed with both of these instrument systems.

2.1 CURRENT METERS

An expanded view of the JASIN area is shown in Figure 2.2. The W1 mooring was located at the Fixed Intensive Array (FIA), near the center of the hydrographic survey grid. The bottom depth there is about 1600 m. The Rockall Bank is southwest of the FIA, and is probably a major source of internal tides observed at the FIA.

The mooring collected data during the period 29 July to 7 September, 1978. It was supported by a subsurface float. Twenty-three vector averaging current meters (VACMs)

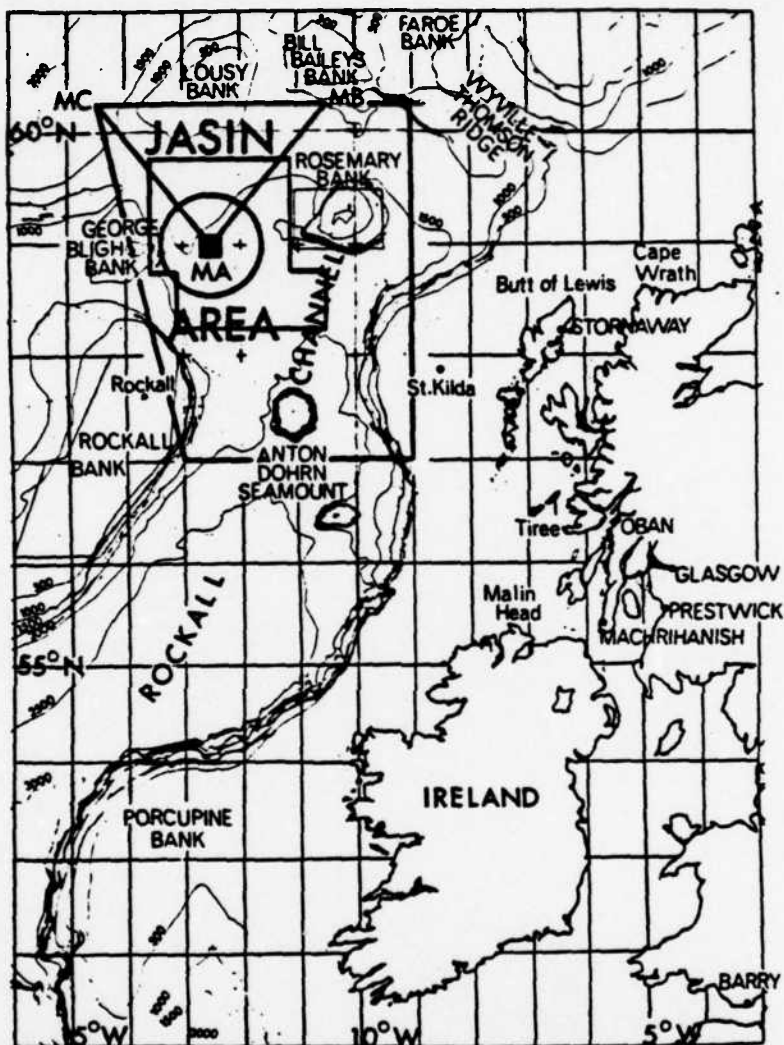


Figure 2.1. The JASIN area in relation to the British Isles. Five regions are shown. The outer quadrilateral is the large scale area, the z-shaped area is the hydrographic survey area, the meteorological triangle is indicated by MA-MB-MC, the circle is the Oceanographic Intensive Area, and the black square is the Fixed Intensive Array. Bathymetry is in meters.

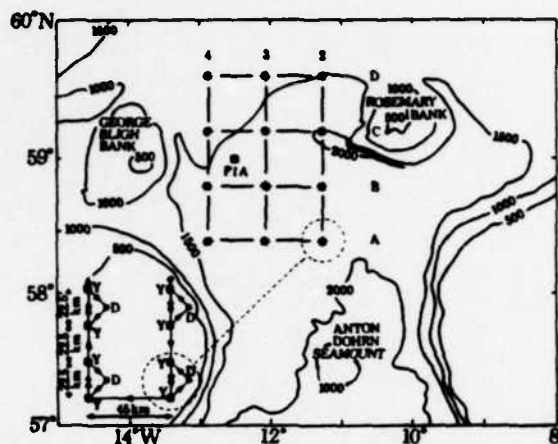


Figure 2.2 JASIN 1978 hydrographic survey area. Isobaths are in meters. The W1 mooring was located in the Fixed Intensive Array (FIA). The Tydeman covered hydrographic stations arranged in a 3x4 grid, with columns labeled 2, 3, and 4, and rows labeled A, B, C, and D. The grid points are 45 km apart. The inset shows the pattern of stations at each grid point. A deep station (D) was worked at the nominal grid position and two yo-yo stations (Y) were each worked twice. From Prangsma et al., 1983.

were attached to it. Sixteen of these were spaced at 3 m intervals from 79 to 124 m depth, and the rest were at 195, 200, 210, 295, 300, 310, and 1000 m depth.

The VACM uses a Savonius rotor and a vane to measure speed and direction, relative to an internal compass. The average current vector is recorded at a sampling rate of 32 per hour. The VACM also has a temperature sensor, and some of the VACMs carry an additional pressure sensor, or a pair of thermistors separated by 1.7 m to measure the vertical temperature difference. Additional technical information on the VACM can be found in McCullough (1975), and the W1 mooring is described by Tarbell, Briscoe, and Weller (1979).

Because there is evidence of mooring motion contamination at the highest frequencies (≥ 4 cph), and because in any case the contribution of high frequencies to the total shear variance is negligible, a low-pass filter was applied to all of the time series (current, temperature, temperature difference, and pressure). The filter had a cut-off frequency of 2.5 cph, and the resultant time series were subsampled at a rate of 8 per hour. Plots of the filtered time series were virtually indistinguishable from the original series.

2.2 CTD SURVEYS AND VAISALA PROFILES

During JASIN, the Dutch oceanographic vessel Tydeman made eight surveys of the hydrographic grid shown in Figure 2.2. At each grid point, the Tydeman performed a triangular station pattern, with one deep CTD cast at the

nominal grid position, and two yo-yo stations (22.5 km apart) were each worked twice. Surveys 1-4 were from 17 July to 10 August and Surveys 5-8 were from 21 August to 14 September.

In Section 4, a statistical model of shear is applied to the current meter data from the W1 mooring. Mean-square shear is related to the mean-square Vaisala frequency. Because there were no salinity sensors deployed on the W1 mooring, it is natural for us to examine the possibility of using temperature alone to reconstruct the Vaisala frequency. To this end, we analyze the separate contributions of salinity and temperature gradients to the Vaisala frequency, in Section 2.2.1. We find that salinity sometimes contributes significantly and nonuniformly to the Vaisala frequency. Therefore, the temperature sensors deployed on the W1 mooring cannot be used reliably to compute the time-dependent Vaisala frequency.

We are forced to use nearby CTD casts to generate temporally and spatially averaged profiles of Vaisala frequency. These averaged profiles are discussed in Section 2.2.2.

2.2.1 Salinity and Temperature Gradient Contributions to Vaisala Frequency

Figure 2.3 shows temperature, salinity, and σ_t in the upper 400 dbar from a representative CTD profile. It is not immediately obvious from these profiles how salinity and temperature gradients contribute to the density stratification. Therefore we have computed the contributions to the Vaisala frequency due to salinity and temperature gradients separately, and combined. The formula σ_t from Mamayev (1975) is convenient for this purpose;

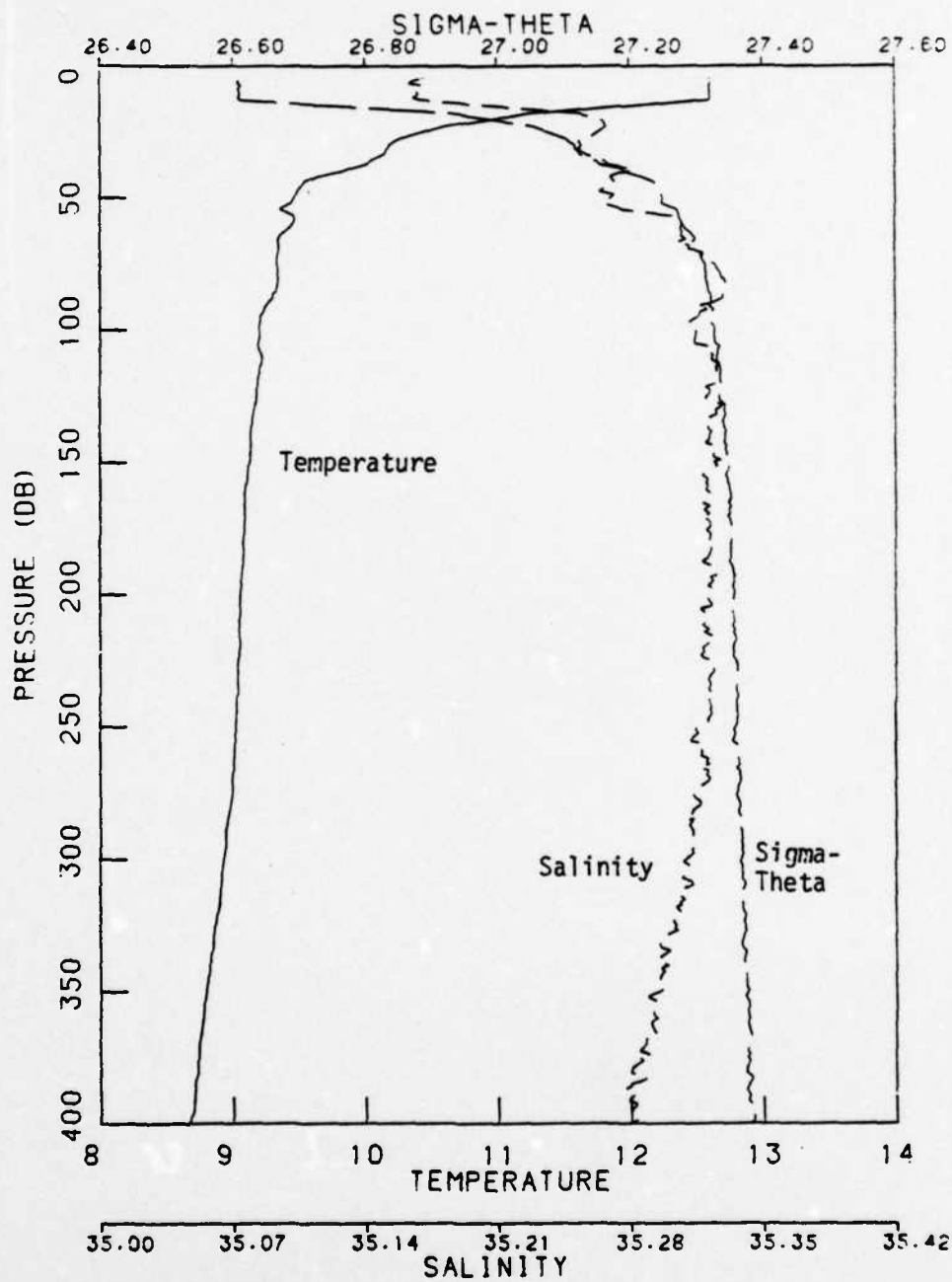


Figure 2.3 CTD profile on August 7, at 02:35 GMT, taken from the Tydeman.

$$\sigma_t = 28.152 - 0.0735T - 0.00469T^2 + (0.802 - 0.002T)(S - 35), \quad (2.1)$$

where T is temperature in $^{\circ}\text{C}$, and S is salinity expressed in parts per thousand. We express the total density gradient in terms of partial derivatives,

$$\frac{d\sigma_t}{dz} = \left(\frac{d\sigma_t}{dz}\right)_T + \left(\frac{d\sigma_t}{dz}\right)_S = \frac{\partial\sigma_t}{\partial T} \frac{\partial T}{\partial z} + \frac{\partial\sigma_t}{\partial S} \frac{\partial S}{\partial z}. \quad (2.2)$$

Using the expression (2.1), the two terms in (2.2) become

$$\begin{aligned} \left(\frac{d\sigma_t}{dz}\right)_T = & - [0.0735 + 0.0938T \\ & + 0.002(S - 35)] \frac{\partial T}{\partial z}, \end{aligned} \quad (2.3)$$

$$\left(\frac{\partial\sigma_t}{\partial z}\right)_S = (0.802 - 0.002T) \frac{\partial S}{\partial z}. \quad (2.4)$$

With the convention that the z -coordinate is positive downwards, the Vaisala frequency N is defined by

$$N^2 = \frac{g}{\rho} \frac{d\rho}{dz}, \quad (2.5)$$

where $\rho = 1 + \sigma_t/1000$ is the total mass density and g is the acceleration due to Earth's gravity. We could rewrite (2.5) in the form

$$N^2 = \frac{g}{1000 + \sigma_t} \left[\left(\frac{d\sigma_t}{dz} \right)_T + \left(\frac{d\sigma_t}{dz} \right)_S \right] . \quad (2.6)$$

Equation (2.6) in conjunction with (2.3) and (2.4) gives the desired result, namely, an expression for the density gradient in terms of the separate contributions due to the temperature and salinity gradients.

Figure 2.4 shows a profile of total Vaisala frequency, as well as the separate contributions from the temperature and salinity gradients. When exhibited in this manner, the total Vaisala frequency is the square root of the sum of the squares of the two separate contributions. Negative values of Vaisala frequency result from our convention that, when we take the square root of (2.6), we retain the sign;

$$N = \text{sign}(N^2) \cdot (|N^2|)^{1/2} . \quad (2.7)$$

In Figure 2.4, we see that the temperature gradient dominates in the upper 60 m. Below that depth, salinity gains in importance, and in certain depth intervals, salinity becomes the dominant factor.

This result is quite typical of the set of CTD profiles that were examined. Of course, details were different from one individual profile to the next. However, one can conclude that below 80-100 m, neither temperature nor salinity is sufficient by itself as an estimator of the density gradient.

We conclude that temperature gradients alone, computed from the thermistors plotted in the moored current

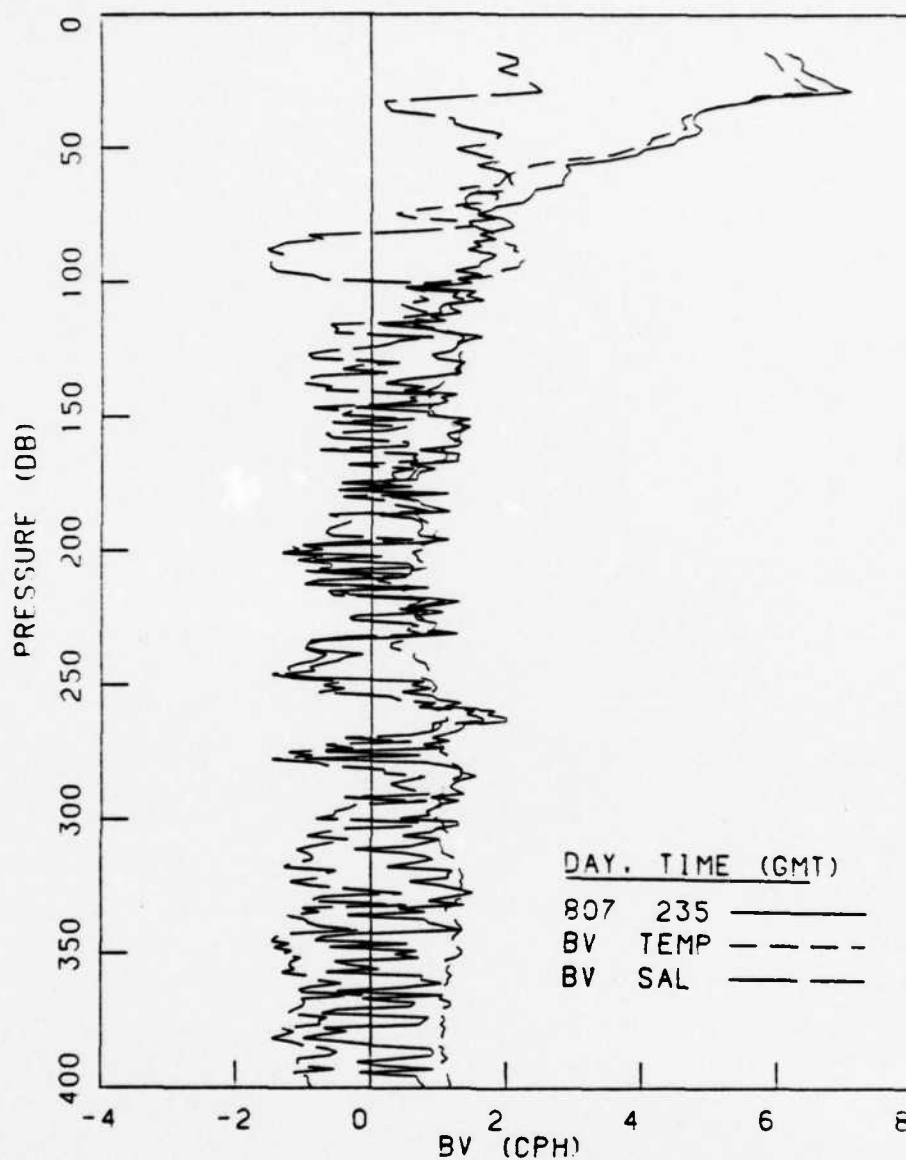


Figure 2.4 Vaisala frequency profile, from CTD cast on August 7 at 02:35 GMT. Solid curve is the total Vaisala frequency, short-dashed curve is the temperature gradient contribution, and the long-dashed curve is the salinity gradient contribution. Above 60 m, most of the density stratification is due to the temperature gradient alone.

meters, cannot be used to estimate density gradients at depths below about 80 m. Instead, we have used the CTD profiles directly, to obtain estimates of the stratification. Our method is described in the following section.

2.2.2 Average Vaisala Frequency Profiles

Figure 2.5 shows the mean profiles of Vaisala frequency for each of the eight Tydem surveys. There was a considerable amount of variability from one survey to the next. The variability is somewhat greater during the first four surveys.

Because there was a two-week gap in the CTD coverage between surveys 4 and 5, we can conveniently group the surveys into two periods. Period 1 was from 31 July to 9 August and included surveys 1 to 4, and Period 2 was from 23 August to 6 September and included surveys 5 to 8.

During Period 1 there were nine CTD casts in the vicinity of the W1 mooring, at grid points B3, B4, C3, and C4 (see Figure 2.2). These grid points are approximately 33 km from the mooring. During Period 2 there were ten CTD casts located at these grid points. For each of these casts the N^2 profile was computed using (2.6). Individual N^2 profiles exhibited considerable finestructure variability. Most finestructure features were probably short-lived compared to the durations of Periods 1 and 2. Also, it is unlikely that finestructure features were coherent over the 33 km separation from the W1 mooring. Therefore, each N^2 profile was filtered, to diffuse the finestructure variability. A 40 m overlapping rectangular weighting function was used. Then the filtered profiles were interpolated onto a uniform 1 m mesh, and separately averaged for both of the periods.

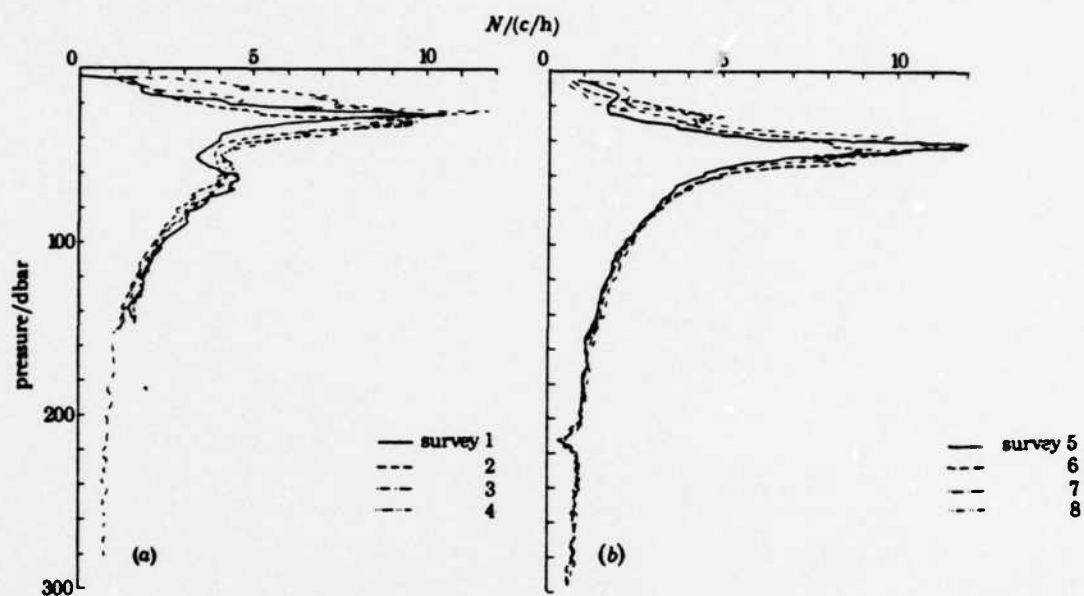


Figure 2.5 Vaisala frequency N , for mean profiles in (a) period 1 and (b) period 2. From Prangma et al., 1983.

Figure 2.6 shows the averaged Vaisala frequency profiles for each of the two periods. In the upper 150 m, the average stratification was slightly higher during Period 2. Below 150 m the profiles were essentially identical. In Section 4, mean-square Vaisala frequency is compared against mean-square shear at discrete depths ranging from 79 to 124 m, from 195 to 210 m, and from 295 to 310 m. Only in the uppermost range, 79 to 124 m, does the Vaisala frequency change appreciably from Period 1 to Period 2.

Of course, there is uncertainty associated with the fact that the CTD casts were located 33 km from the mooring. It is difficult to quantify this uncertainty. No systematic trends could be discerned in the profiles from any of the grid points, and none of the grid point locations could be characterized, as a class, as having weaker or stronger stratification than the other locations.

In the upper 100 m, Vaisala profiles taken from adjacent grid points within twelve hours of each other sometimes differed significantly. These differences could probably be attributed to vertical displacements associated with low frequency internal waves.

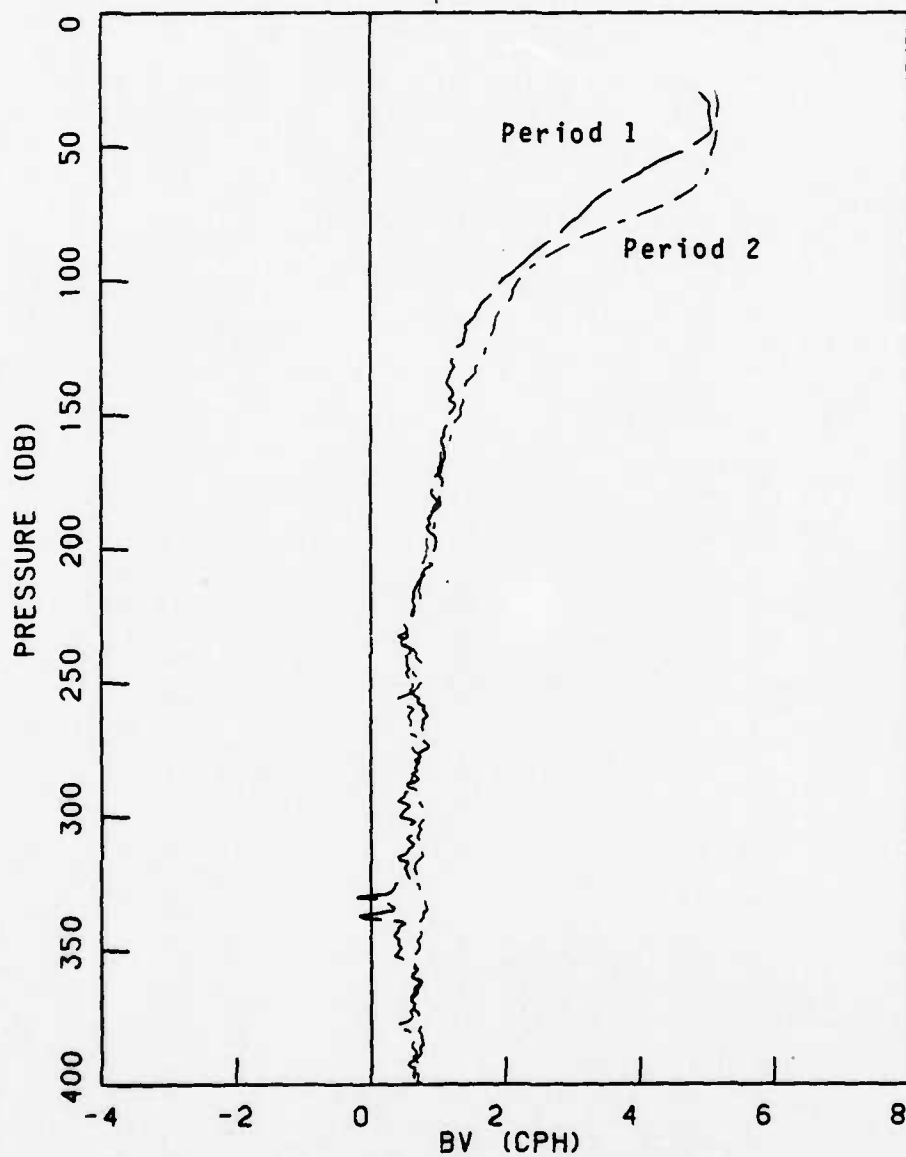


Figure 2.6 Brunt-Vaisala frequency profiles, averaged over Period 1 (31 July to 9 August) and Period 2 (23 August to 6 September).

Section 3

DETERMINISTIC DESCRIPTION OF CURRENT AND SHEAR

During JASIN a significant component of the shear was rotary in nature. The tip of the shear vector rotated clockwise at the semidiurnal frequency and traced an elliptical orbit, with an amplitude and an eccentricity that varied continuously. Clearly, this deterministic component of shear is associated with the semidiurnal internal tide. Before we proceed with a deterministic description of the shear field, we begin with a description of the current field, for two reasons. First, shear measurements are derived from current observations. The current field is simpler to understand intuitively, and deterministic analysis techniques applied to currents are probably more familiar to most readers. Second, the local internal tide is generated by an imperfectly understood interaction between the barotropic tidal current and a nearby steeply sloped bottom feature. Therefore, we are justified in looking for a descriptive relationship between the variability of the shear field and the barotropic tidal current field.

3.1 CURRENT FIELD

Figure 3.1 shows the current at 124 m depth, projected onto four coordinate frames, each rotated by successive 45° angles counterclockwise with respect to east. Thus, the records labelled 0 and 90 are the eastward and northward components, respectively. The velocity is dominated by the M_2 semidiurnal tide, with a period of 12.4 hr. The peak-to-peak amplitude of the tide varies, but is on the order of 20 cm s⁻¹.

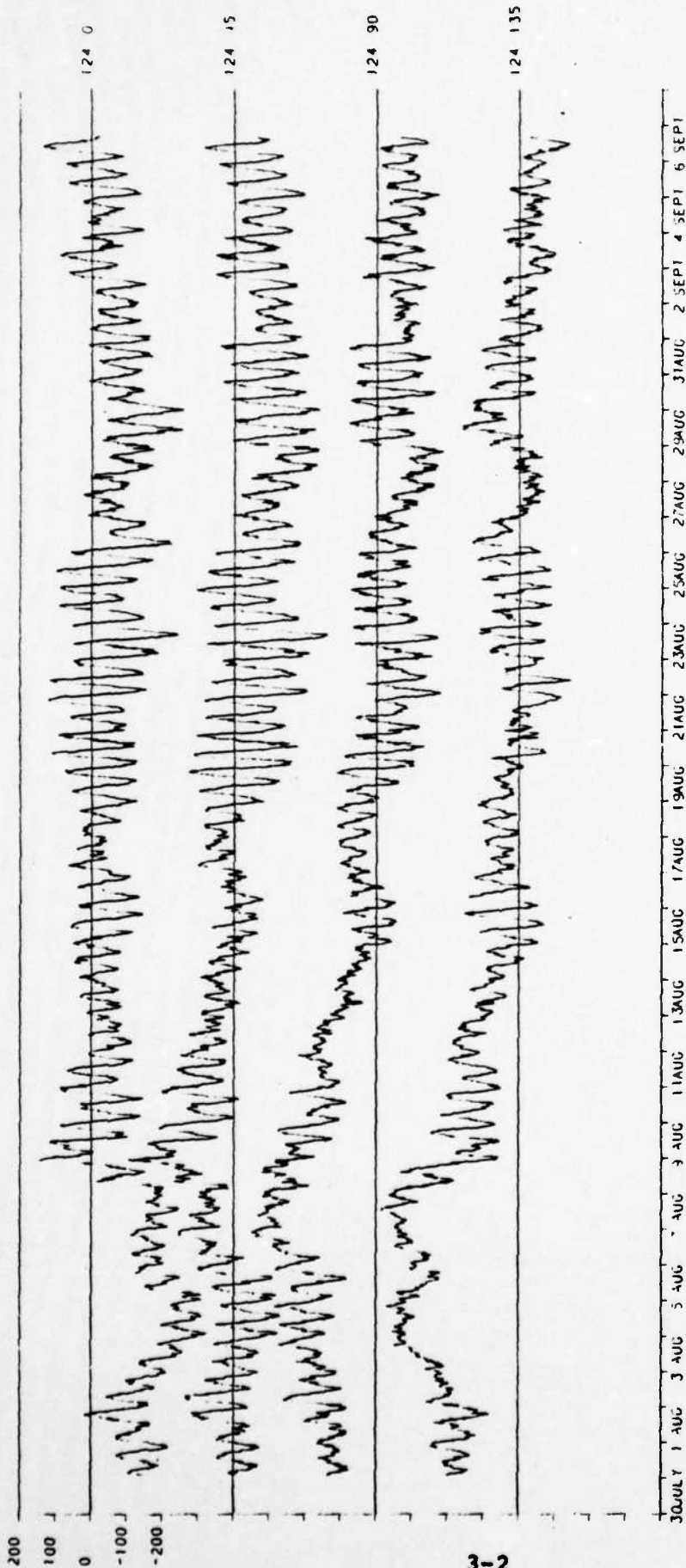


Figure 3.1 Current at 124 m depth from the JASIN W1 mooring, projected onto four coordinate frames. Each frame is rotated by successive 45° angles CCW with respect to east. Thus the records labeled 0 and 90 are eastward and northward velocity components, respectively. Units are mm/sec.

By projecting the velocity onto four coordinate frames, certain aspects of its tidal oscillation are emphasized. We find that the tidal oscillations exhibit strong variability. During the period 3-5 August for example, the 45° projection shows strong tidal oscillations, while the 135° projection does not exhibit a noticeable oscillation. Therefore, we infer from this result that the elliptical orbit of the tidal velocity vector is exceedingly eccentric--perhaps even linear--and the major axis is oriented parallel to the 45° direction. During the period 12-14 August, tidal oscillations are just barely discernable in the 90° projection. We infer that the tidal elliptical orbit is but slightly less eccentric, and the major axis is aligned parallel to 0° . During the period 23-25 August the four velocity projections show nearly equal amplitude tidal oscillations. There is a small directional preference for 45° . Therefore, we infer that the tidal elliptical orbit is nearly circular.

Not only are the tidal oscillations variable in character, but also the low frequency component of the current is strongly variable. The low frequency component is quite strong from 31 July to mid-August, and much weaker thereafter. During the beginning of August, the direction of this low frequency component is toward the northwest, and toward the end of August the direction shifts to the southwest. These low frequency components result from mesoscale eddy circulations. Pollard (1983) found that the mesoscale field in the hydrographic survey area was dominated by a cold anticyclonic eddy which moved westward across the northern half, and an anticyclonic meander of warmer water in the southern half. In addition, there were several smaller cyclonic circulations which were not well resolved.

Figure 3.2 shows an analysis of dynamic height at a depth of 200 db. At the location of the FIA (59°N, 12.5°W), the observed current shifts from 24 cm s⁻¹ toward the northwest during Survey B to 3 cm s⁻¹ toward the southwest during Survey C. This variation can be attributed to the geostrophic current associated with the changing mesoscale field.

Figure 3.3 shows the spectral density of the current at 79 m depth. Two components are shown; the clockwise (CW) rotary component is indicated by the dashed curve, and the counterclockwise (CCW) rotary component by the solid curve. The sharp peak is at the semidiurnal tidal frequency, 0.0805 cph, which corresponds to a period of 12.42 hr. The power of the CW rotary tidal component is about four times that of the CCW component. Therefore the amplitude is greater by a factor of about two. If the current vector described a CW circular orbit, then the CCW rotary component would vanish. If the current vector described a linear oscillation, then the CW and CCW components would be equal in amplitude.

In general, the current vector can describe an ellipse whose ratio of minor axis to major axis, A , lies somewhere in the range $0 < A < 1$. We can quantify A in terms of the CW and CCW components as follows. Consider a current vector $u(t) + iv(t)$ with a CW elliptical orbit

$$u + iv = \cos \omega t - iA \sin \omega t, \quad (3.1)$$

where ω is the angular frequency. The major axis is of unit length along the x-axis, and the minor axis is of length A along the y-axis. Equation (3.1) can be rewritten

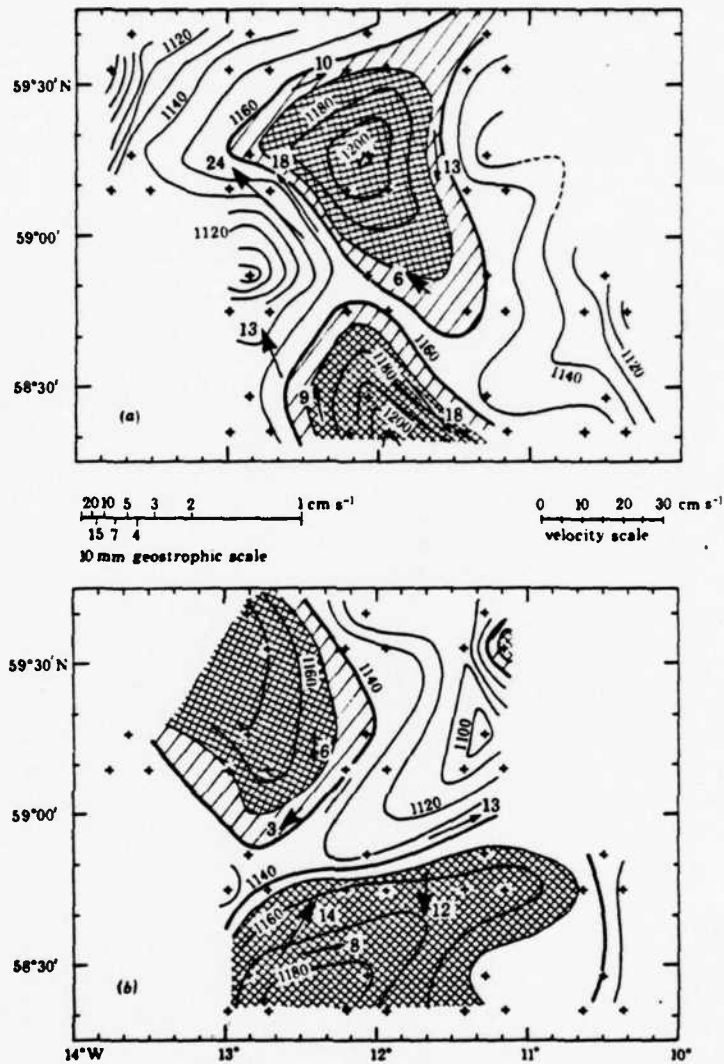


Figure 3.2. Dynamic heights (dynamic mm) at 200 dbar adjusted to a level of no motion at the bottom. Light arrows show estimated geostrophic velocities and heavy arrows show 200 m current observations. From Pollard (1983). (a) Survey B, 31 July to 11 August 1978. (b) Survey C, 20-29 August 1978. Plus marks indicate hydrographic stations from the Challenger survey.

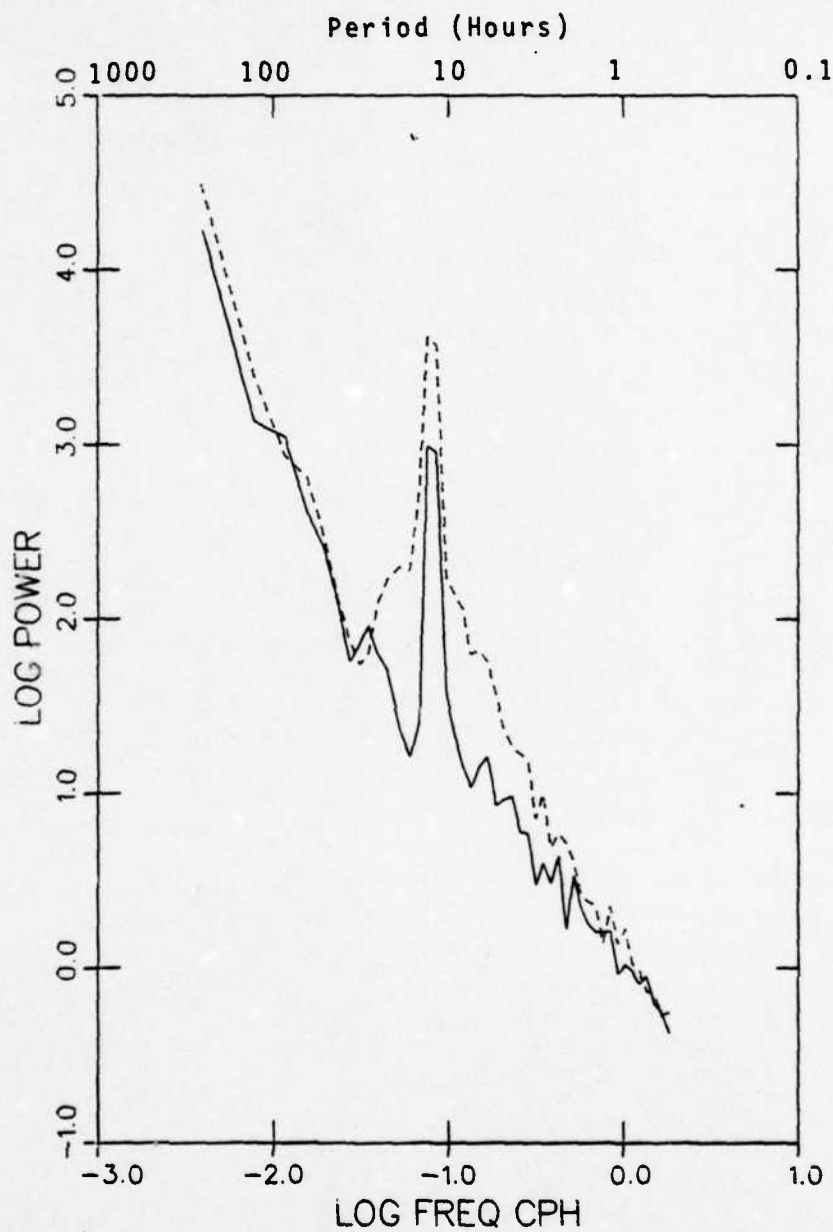


Figure 3.3. Power spectral density of 79 m current. Solid curve indicates rotary CCW component, dashed curve indicates CW component.

$$u + iv = \frac{1+A}{2} e^{-i\omega t} + \frac{1-A}{2} e^{i\omega t} , \quad (3.2)$$

which is the sum of a CW rotary component of amplitude $(1+A)/2$, plus a CCW component of amplitude $(1-A)/2$.

Thus, the ratio R of the amplitudes of the CCW to CW rotary components is simply

$$R = \frac{1-A}{1+A} , \quad (3.3)$$

and A in terms of R is

$$A = \frac{1-R}{1+R} . \quad (3.4)$$

In the example in Figure 3.3, the ratio of the average rotary amplitudes is $R = 1/2$, and therefore the ratio of the average minor and major axis lengths is $A = 1/3$.

Figure 3.4 is a variance preserving plot of the 79 m current power spectrum. Again, the two rotary components are shown separately. The narrow frequency band centered at the semidiurnal frequency contains most of the energy.

A technique called complex demodulation is useful for analyzing the time-dependent amplitude and phase of the current in the semidiurnal frequency band. This technique is described in Appendix A. Its purpose is to demodulate a vector time series. We use it here to separate out the CW and CCW rotary components in the near-semidiurnal frequency band. Figure 3.5 shows the time dependent rotary components of the current at 79 m depth. The CCW amplitude ranges from

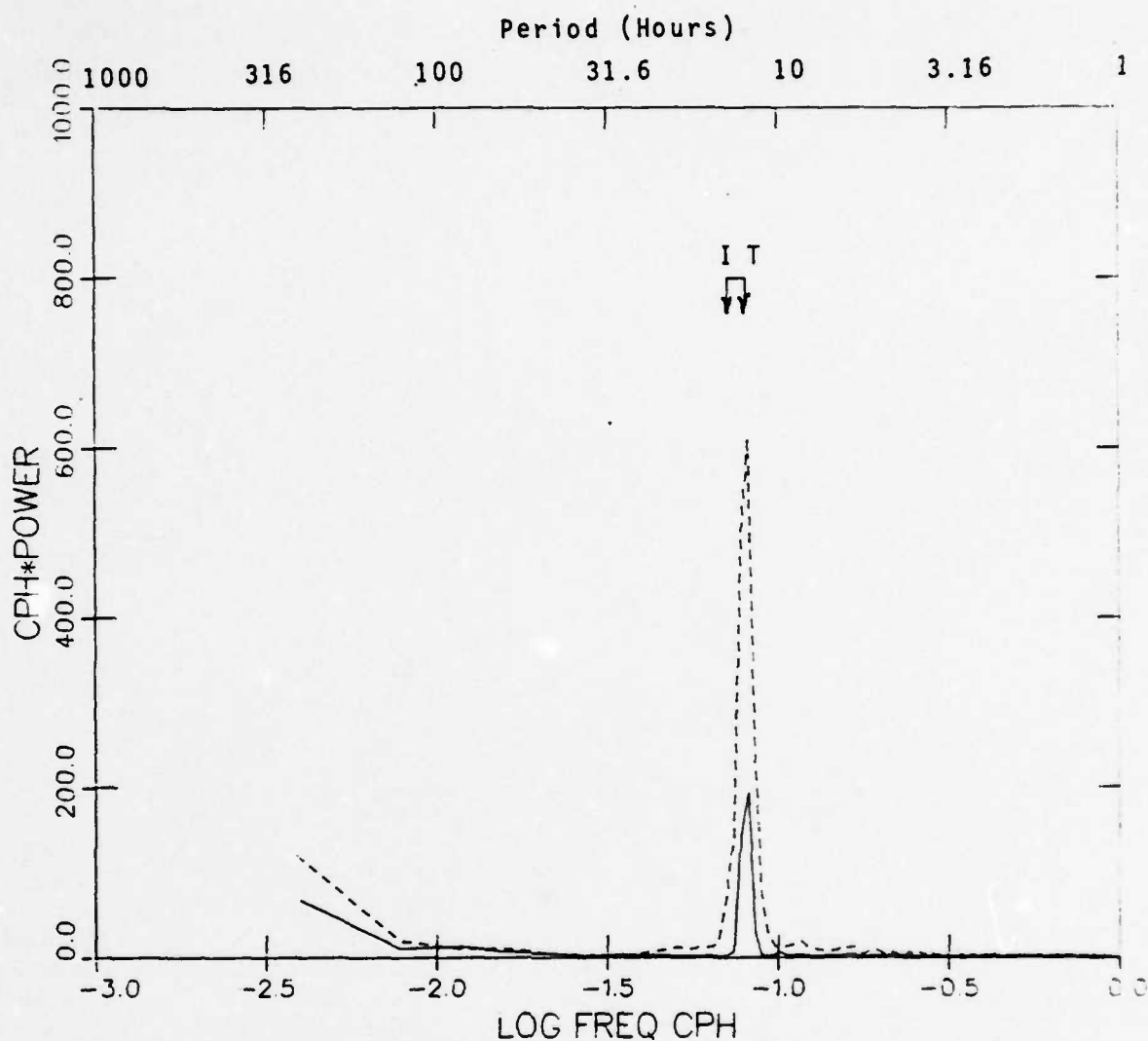


Figure 3.4. Power spectrum of 79 m current, in variance preserving form. Solid and dashed curves indicate CCW and CW rotary components, respectively. Arrows labeled I and T indicate inertial and semidiurnal tidal frequencies, respectively.

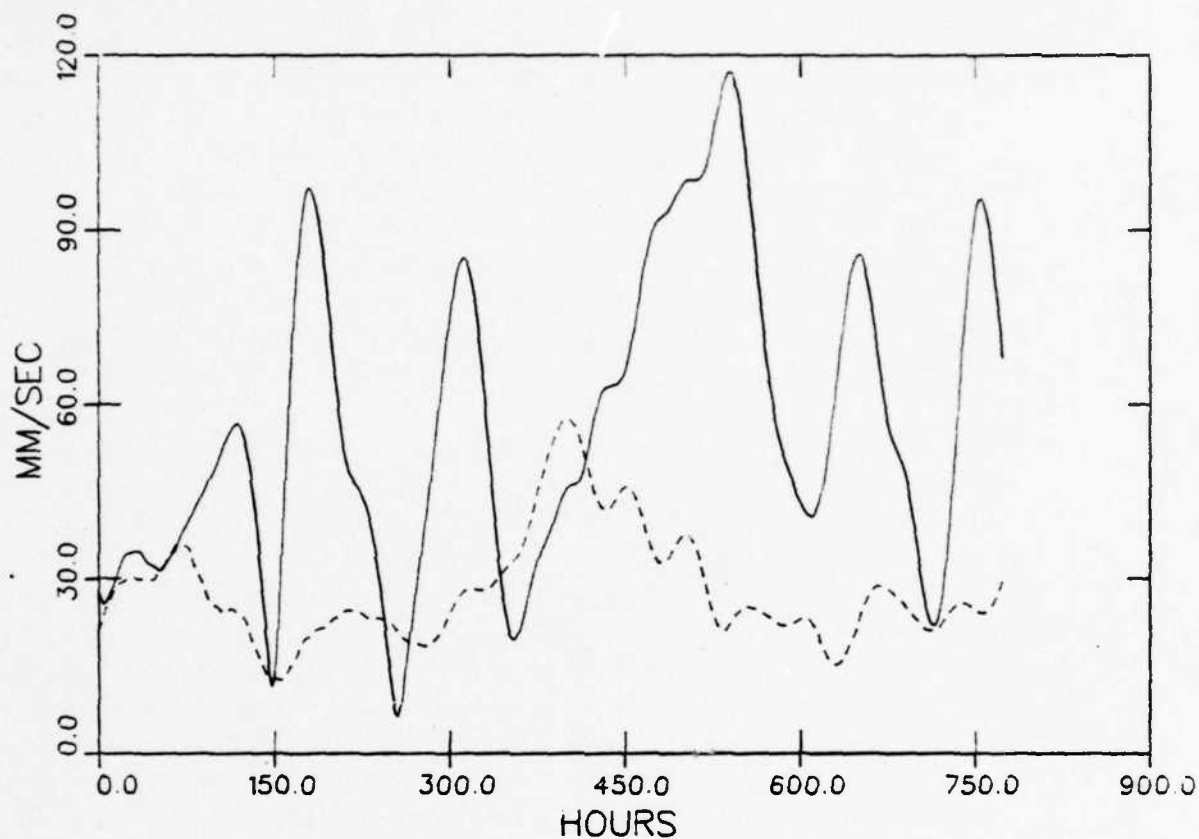


Figure 3.5. Amplitudes of clockwise (solid) and counter-clockwise (dashed) rotary components of 79 m current, at the semidiurnal tidal frequency.

15 to 55 mm/sec, and the CW amplitudes ranges from 10 to 115 mm/sec. The CCW amplitude varies rather smoothly, while the CW amplitude is transient in character. The CCW rotary component probably represents a base state, largely due to the barotropic tide. Careful observation reveals that the CCW amplitude is cyclic in character, with a period of about 350 hours. This period corresponds to that produced by intermodulation between the principal lunar (M_2 period = 12.42 hr) and the principal solar (S_2 period = 12.00 hr) tidal constituents.

During intermittent intervals, the CW component undergoes transient bursts, above the level of the CCW component. We will see in Section 3.2 that these bursts represent transients in the internal baroclinic tide, because the internal tide velocity vector is predominantly CW rotary. Figure 3.6 shows the ratio A of the minor to major axes, for the tidal ellipse at 79 m depth. The ratio A is computed from the ratio R of the rotary amplitudes, using Equation (3.4). During intervals when the CCW component dominated ($R > 1$), the ratio A was arbitrarily set to zero. During intervals when the CW component dominated, i.e., during outbursts of internal tides, the ratio A increased to levels in the range 0.4 to 0.7.

Figure 3.7 shows the u-component of current at four depths; 79, 124, 200, and 300 m. The current is remarkably coherent over this depth range. The reason for this coherence is the strong dominance of two constituents of the current field, the barotropic tide and the low frequency mesoscale motion. Close inspection of this plot shows that the internal wave field tends to degrade the vertical

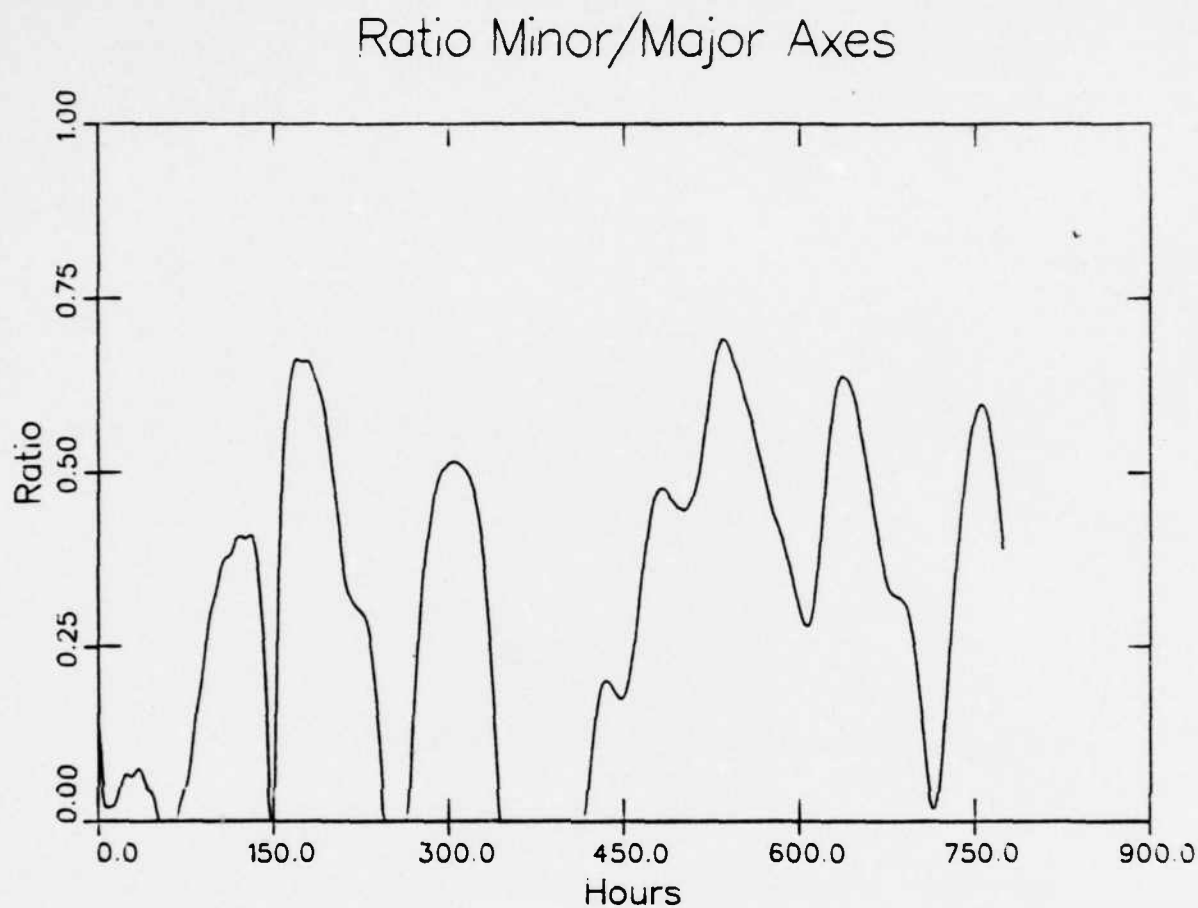


Figure 3.6. Ratio of minor to major axes, for tidal ellipse described by 79 m current. Ratio = 1 indicates that the current describes a clockwise circle. Ratio = 0 indicates that the tide describes a linear orbit (clockwise and counterclockwise rotary components are equal in amplitude).

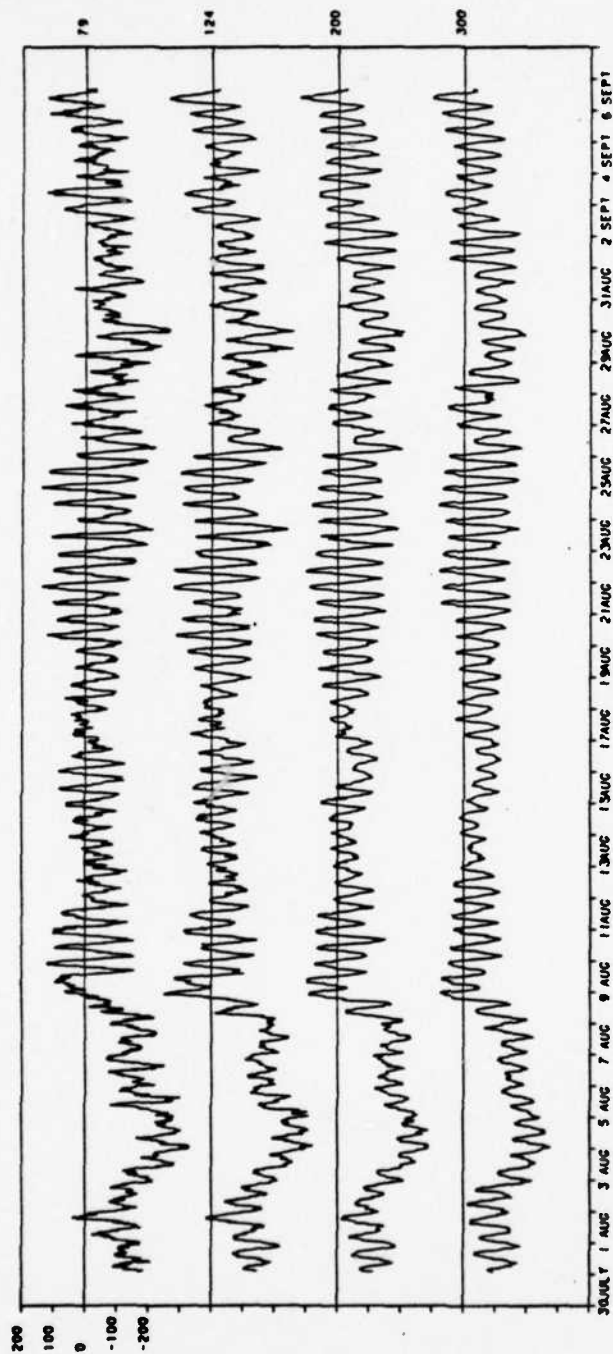


Figure 3.7. Time series of u-component of velocity at four depths; 79, 124, 200, and 300 m. Units are mm/sec.

coherence. High frequency oscillations at 79 m (in the internal wave frequency range, up to the Vaisala frequency ~ 4 cph) are stronger than oscillations at greater depths, where the Vaisala frequency is lower. Also variations are apparent between the current at different depths at the semidiurnal frequency. These variations are manifestations of the internal tide, and are emphasized in Section 3.2.

3.2 SHEAR FIELD

Figure 3.8 shows the u-component of velocity difference across the depth intervals 91-94 m, 94-97 m, 97-100 m, and 100-103 m. During the first third of each time series, the low-frequency components show considerable meso-scale activity. Semidiurnal oscillations intermittently became active during various portions of the time series. These oscillations are evidence of internal tides; since their semidiurnal frequency is higher than the local inertial frequency, they are free to propagate through the ocean as internal waves. In addition, signals associated with higher frequency internal waves are present throughout the time series.

In general, the shear does not appear to have the high vertical coherence, shown by the current. There are a few exceptions; for example the events that occur on 29 August, and to a lesser degree, at the end of 15 August. For the most part however, short term events show little correlation among the shear records.

Across large vertical separations, the near-semidiurnal frequency band of velocity difference is completely dominated by CW rotary oscillations. This is clearly

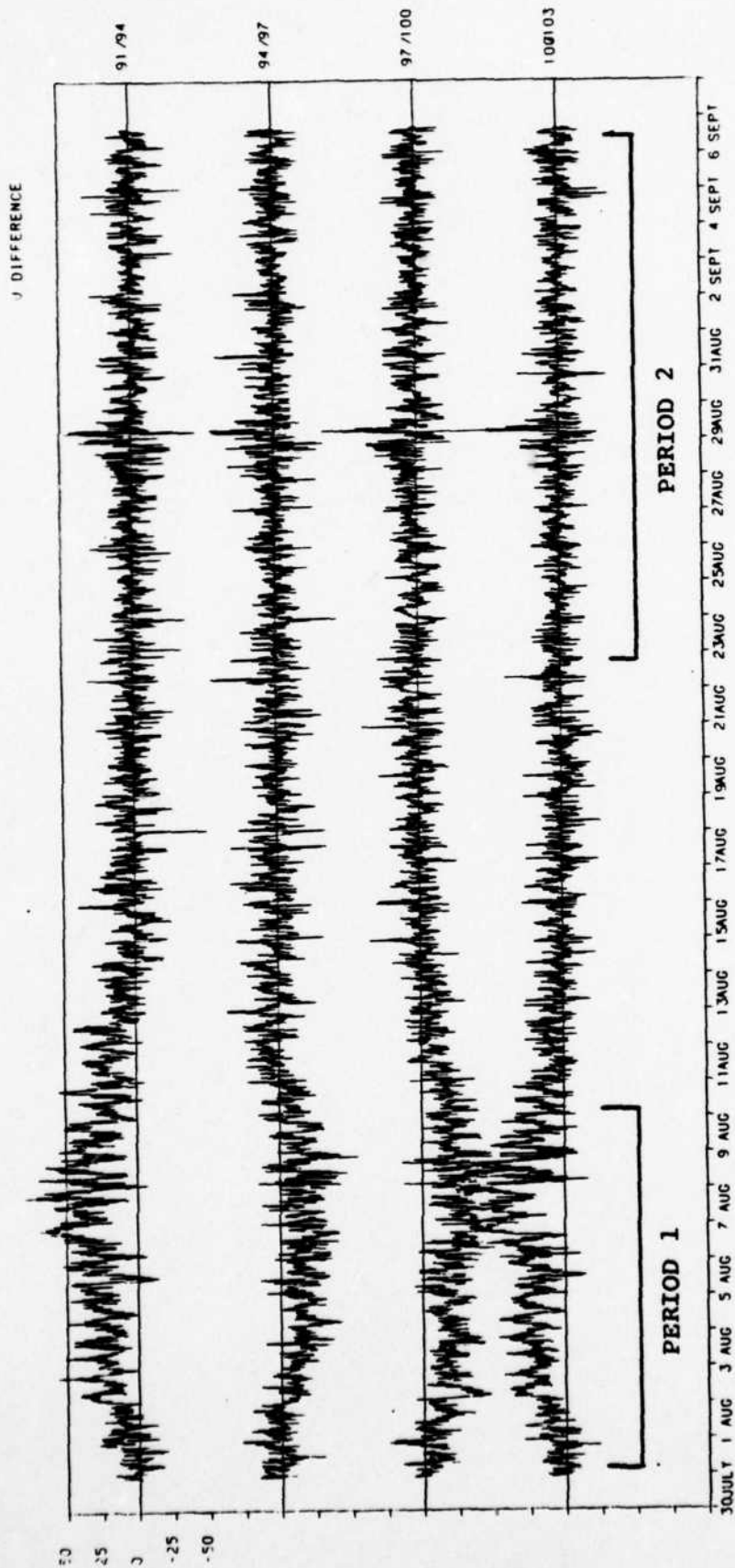


Figure 3.8. Time series of u-component of velocity difference over depth intervals 91-94 m, 94-97 m, 97-100 m, and 100-103 m. Units are in mm/sec. Note the low-frequency mesoscale activity during the beginning of the records.

shown in Figure 3.9, which is a plot of spectral density of velocity difference across the vertical interval 79-124 m. The CW rotary component is elevated above the CCW component over the frequency band 0.037 to 0.37 cph. This is no sign of a spectral peak in the CCW component at the semidiurnal frequency. The same spectrum is shown in variance preserving form in Figure 3.10. This figure shows that the spectral peak at the semidiurnal frequency is too broad to resolve separately the energy at the inertial frequency. The variance preserving spectral plot emphasizes the relative insignificance of the CCW rotary component of shear.

The complex demodulation of the 79-124 m velocity difference, shown in Figure 3.11, demonstrates the transient nature of the internal tide. Transient internal tides exhibit velocity differences which reach amplitudes of order 40-60 mm/sec, and last over intervals of order 40 to 80 hours. Note that the CW amplitude dominates the CCW amplitude. The reason is that the barotropic tide has been largely removed from the record by the differencing operation. The remaining signal is mostly the baroclinic tide, which has a nearly circular CW orbit.

Let us compare Figure 3.11 with Figure 3.5, which shows the complex demodulation of the 79 m current. Recall that in Figure 3.5 the CCW rotary component probably represents a base state, largely due to the barotropic tide. If we assume that the elliptical orbit of the barotropic tide is strongly eccentric, then the contributions of the CW and CCW rotary components are roughly equal. We infer that the excess of the CW over the CCW amplitude corresponds to the baroclinic tide. The transient peaks in the CW component in

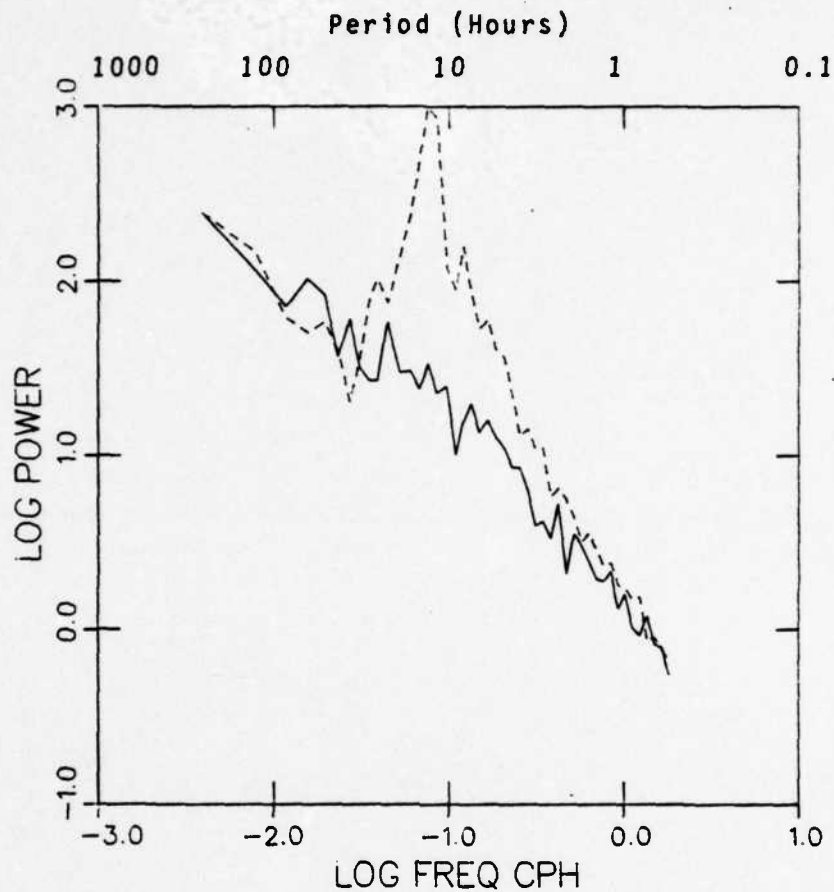


Figure 3.9. Power spectral density of velocity difference across 79-124 m. Solid and dashed curves denote rotary CCW and CW components, respectively.

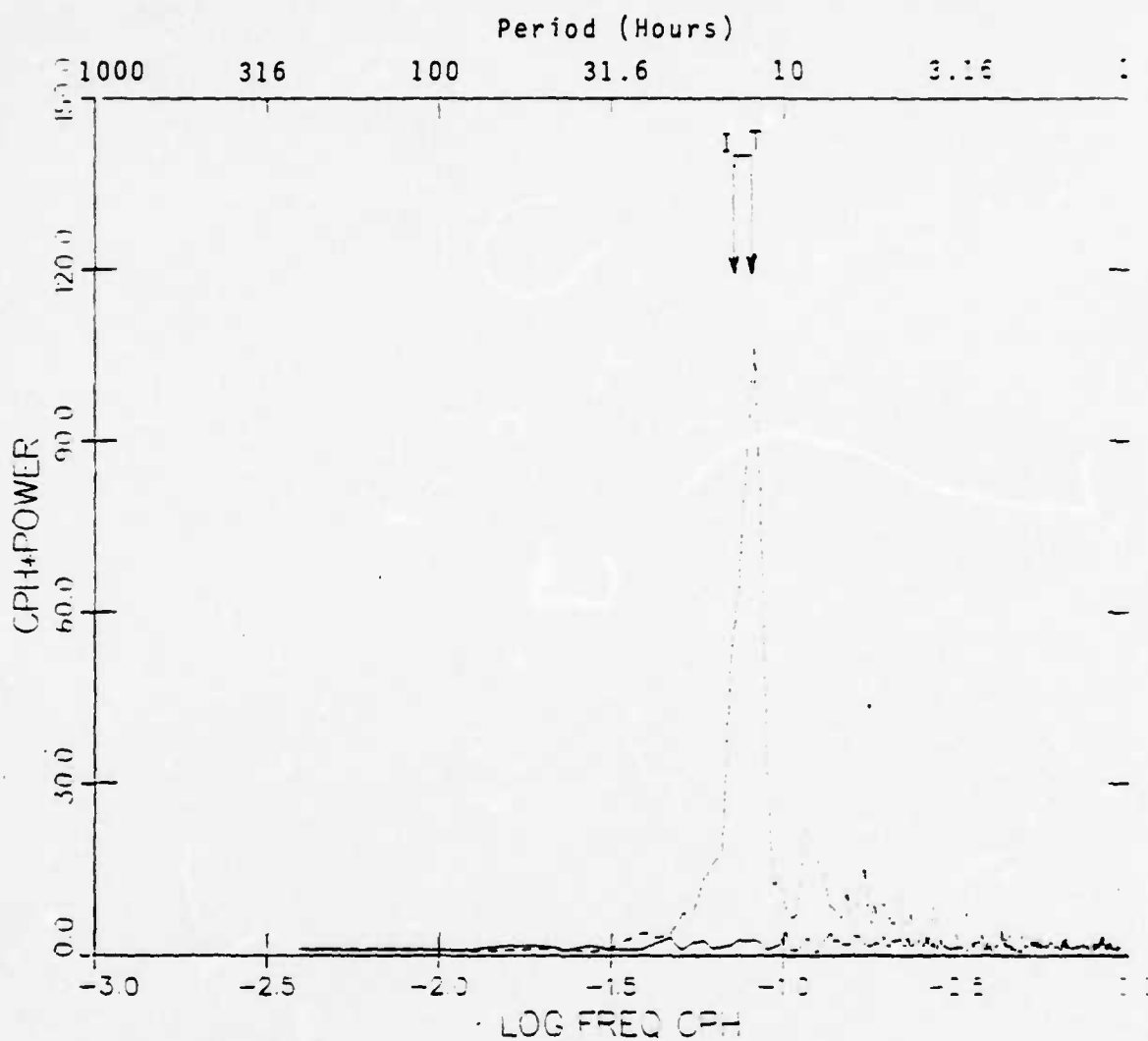


Figure 3.10. Power spectrum of velocity difference across 79-124 m, in variance preserving form. Solid and dashed curves denote rotary CCW and CW components, respectively. Arrows labeled I and T denote inertial and tidal frequencies.

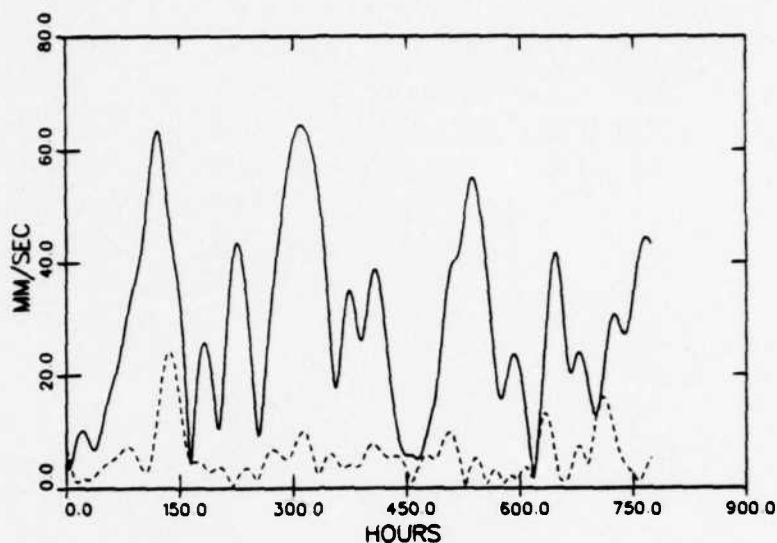


Figure 3.11. Complex demodulation of 79-124 m velocity difference, at the semidiurnal frequency. Solid and dashed curves denote amplitudes of CW and CCW rotary components, respectively.

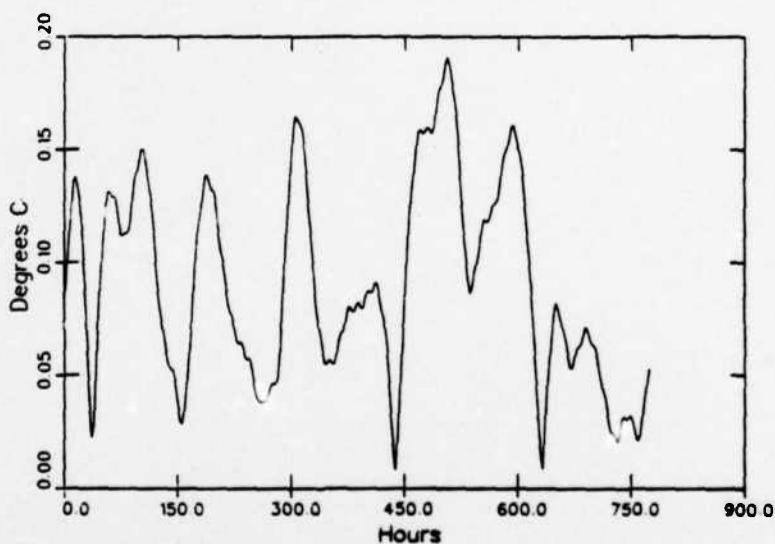


Figure 3.12. Peak-to-peak envelope of semidiurnal temperature oscillations, at 79 m depth. Some of the biggest transient peaks can be correlated with the peaks in velocity difference in Figure 3.11.

excess of the CCW component roughly correspond to the peaks in the CW component of the 79-124 m velocity difference in Figure 3.11.

Figure 3.12 shows a demodulated record of temperature fluctuations, at 79 m depth. This record gives the peak-to-peak envelope of semidiurnal temperature oscillations. The transient peaks are indicative of periods of intense semidiurnal internal tide, due to the vertical displacement of a mean temperature gradient. Several of these peaks, especially those at 120, 300, 500, and 650 hours can be correlated with peaks in CW velocity difference in Figure 3.11. In addition, the peak at 200 hours is correlated with a peak in CW velocity in Figure 3.5. In the presence of a single coherent packet of internal waves, the correlation should be unambiguous. However, the correlation should be degraded in the simultaneous presence of two or more wave packets, propagating in different directions.

Kundu (1976) computed particle orbits of near-inertial waves. His WKB solutions are approximate, and are valid only for environments where the Vaisala frequency profile varies over spatial scales larger than the vertical scales of motion. Since we are considering the upper thermocline where the Vaisala profile varies strongly, the approximation is not particularly good. However, we are not explicitly seeking a quantitative solution, but only some guidance for understanding our results. For the special (but not unduly restrictive) case of horizontal propagation along the x-axis, Kundu (1976) showed that particle orbits are described by

$$u = \mp B \frac{m^{1/2}}{k} \cos (kx \pm \int m dz - \omega t), \quad (3.5)$$

$$v = \mp B \frac{f}{\omega} \frac{m^{1/2}}{k} \sin (kx \pm \int m dz - \omega t) , \quad (3.6)$$

where B is an arbitrary amplitude, ω is angular frequency, f is the inertial frequency, k is the horizontal wavenumber, and m is the vertical wavenumber given by

$$m^2(z) = k^2 \left(\frac{N^2(z) - \omega^2}{\omega^2 - f^2} \right) . \quad (3.7)$$

Equations (3.5) and (3.6) describe a CW ellipse, whose minor to major axis ratio is f/ω . For the case of an internal tide with period 12.4 hr at the latitude of the W1 mooring (where the inertial period is 14.0 hr), this ratio is 0.89.

What will these results imply for the velocity shear across some vertical separation Δz ? We consider a single source of coherent internal waves, propagating through a horizontally homogeneous ocean with depth-dependent stratification. Then the internal wave train arrives at two vertically separated current meters with different amplitudes and relative phases. The amplitude $Bm^{1/2}/k$ will differ because $m(z)$ in Equation (3.7) is depth-dependent. The phase factor $\int m dz$ will differ because of the slightly different characteristic lines followed by internal wave trains before they arrive at different current meters. However, the eccentricity of the particle orbits at each of the current meters is the same; the minor-to-major axis ratio is f/ω . The velocity difference between these current meters is a vector which describes an elliptical orbit with the same ratio f/ω . The amplitude of the major axis is simply

$$\Delta u = (B/k) [m_1 + m_2 - 2(m_1 m_2)^{1/2} \cos \phi]^{1/2} , \quad (3.8)$$

where m_1 and m_2 are the vertical wavenumbers at the respective depths of the two current meters, and ϕ is the relative phase. Moreover, the ellipse orientation (the direction of the major axis) remains aligned along the horizontal direction of wave propagation.

The minor-to-major axis ratio of the 79-124 m velocity difference is shown in Figure 3.13. Periods when the internal tide is particularly strong (when the CW rotary amplitude in Figure 3.11 exceeds 30 mm/sec) are emphasized by the shaded areas. As mentioned above, the expected ratio for a single source of coherent internal tides is 0.89, and is indicated by the dashed line. The observed ratio fluctuates rapidly, but the peak values in the shaded regions range from 0.80 to 0.98. Strong fluctuations are to be expected when multiple trains of internal waves, propagating in various directions, arrive at the mooring simultaneously.

An indication of the direction of propagation of the internal tide was obtained in the following manner. The 79-124 m velocity difference was resolved into four non-orthogonal components; 0° , 45° , 90° , and 135° CCW from due east. These records were then demodulated at the semidiurnal frequency, and the results displayed in Figure 3.14. During each of the seven periods during which the internal tide was intense (shaded periods in Figure 3.13), the direction of the major axis of the shear ellipse was determined from the relative amplitudes of the four components.

In theory, this technique yields the horizontal direction of propagation of the internal tide, and hence the direction of the source of these tides. In practice, the

Ratio Minor/Major Axes (79-124 m)

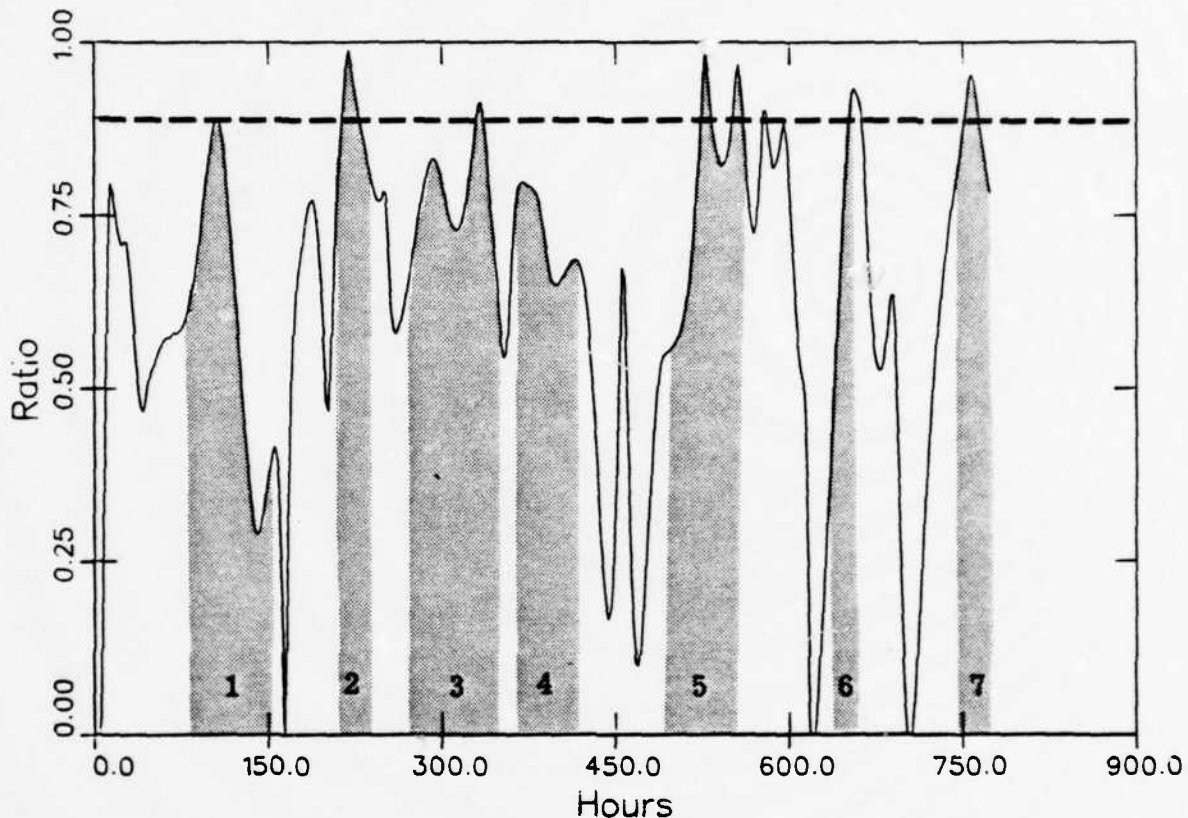


Figure 3.13. Ratio of minor-to-major axes, for tidal ellipse described by 79-124 m velocity difference. Ratio = 1 indicates that the tidal shear describes a clockwise rotary circle. Ratio = 0 indicates that the tidal shear describes a linear orbit (clockwise and counterclockwise rotary components are equal in amplitude). The dashed line indicates Ratio = 0.89, the value expected from theory for a coherent internal wave at tidal frequency. Shaded areas denote periods when the baroclinic tide is particularly intense, and are numbered for reference to Table 3.1.

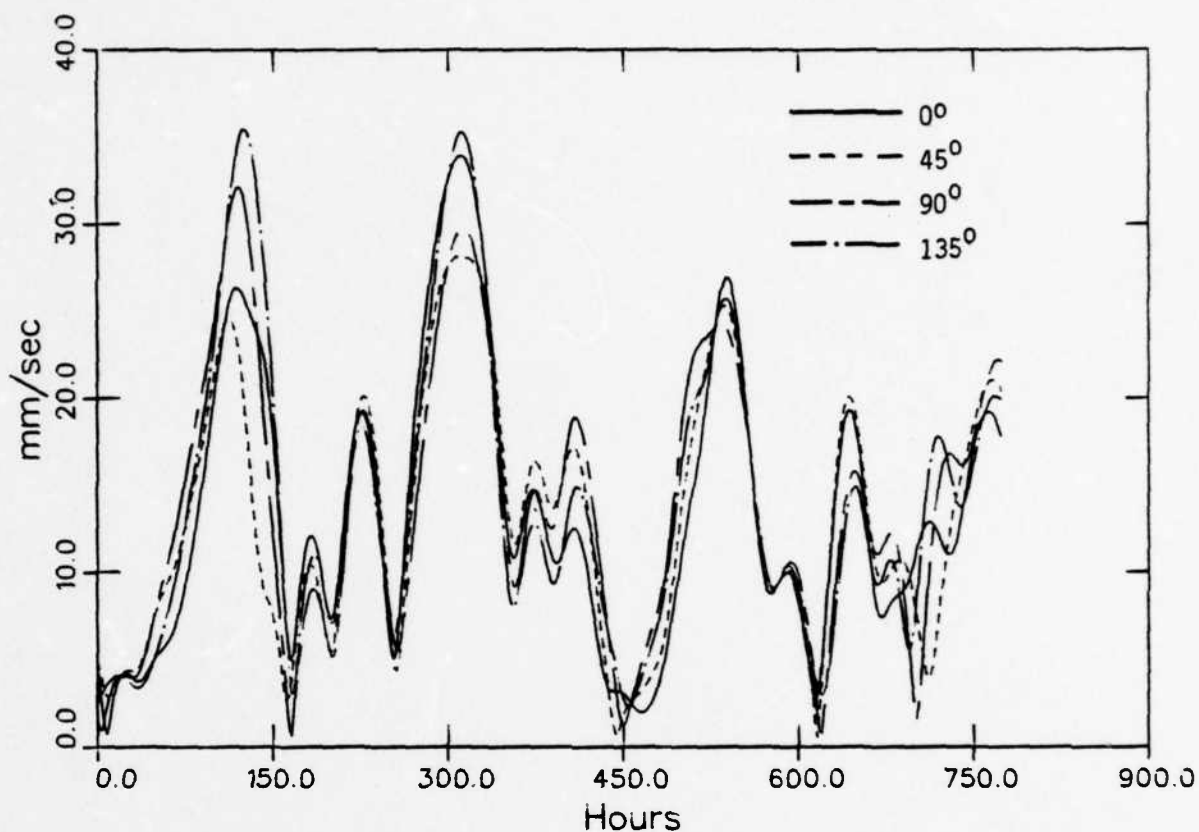


Figure 3.14. Velocity difference across 79-124 m resolved into four components; 0°, 45°, 90° and 135° CCW from due east, and demodulated at the semi-diurnal frequency. The relative strengths of the velocity difference components allows one to measure the orientation of the major axis of the shear ellipse, and hence the direction of propagation of internal tides (indeterminate to within 180°).

results are not unequivocal for three reasons. First, the direction is indeterminate to within 180° . Second, if two or more internal wave packets are present simultaneously with different directions of propagation, neither of the directions can be correctly ascertained. Third, the expected minor-to-major axis ratio, $f/\omega \approx 0.89$, is very close to 1.0. Therefore, it is difficult to measure the shear ellipse orientation in a noisy signal. This effect could be mitigated in the future by performing field experiments at lower latitudes, where the inertial frequency, and hence the ratio f/ω , is smaller.

Table 3.1 is a list of the analysis results. The directions are presented schematically by arrows in Figure 3.15. The lengths of the arrows are roughly proportional to the amplitude of the internal tide. The reader should keep in mind the 180° indeterminacy. However the steepest, closest bathymetric features are most likely the sources of the internal tides. Therefore to resolve the 180° indeterminacy, the arrow directions point to the most probable sources.

Levine et al. (1983) discuss internal tides at JASIN during the one-week period 22-29 August. Using three moorings as an antenna, they concluded from an analysis of temperature records that the internal tide was most likely generated at the Rockall Bank. This time period overlaps Periods 5 and 6 in Table 3.1, which designate the George Bligh and Rosemary Banks as the most likely sources. The reason for this inconsistency is not known, but might stem from the fact that propagation direction tends to vary during the week in question. This directional variation may indicate that more than one wave packet was present. However,

Table 3.1
DIRECTIONS OF PROPAGATION AND MOST LIKELY SOURCES

<u>Period</u>	<u>Direction (CCW of East)</u>	<u>Source</u>
1	110° - 135°	Anton Dohrn Seamount
2	45°	Rockall Bank
3	155° (or 335°)	Hebrides Shelf*
4	60°	Rockall Bank
5	0°	George Bligh Bank
6	205° (or 25°)	Rosemary Bank*
7	60° - 80°	Rockall Bank

* Indicates uncertainty

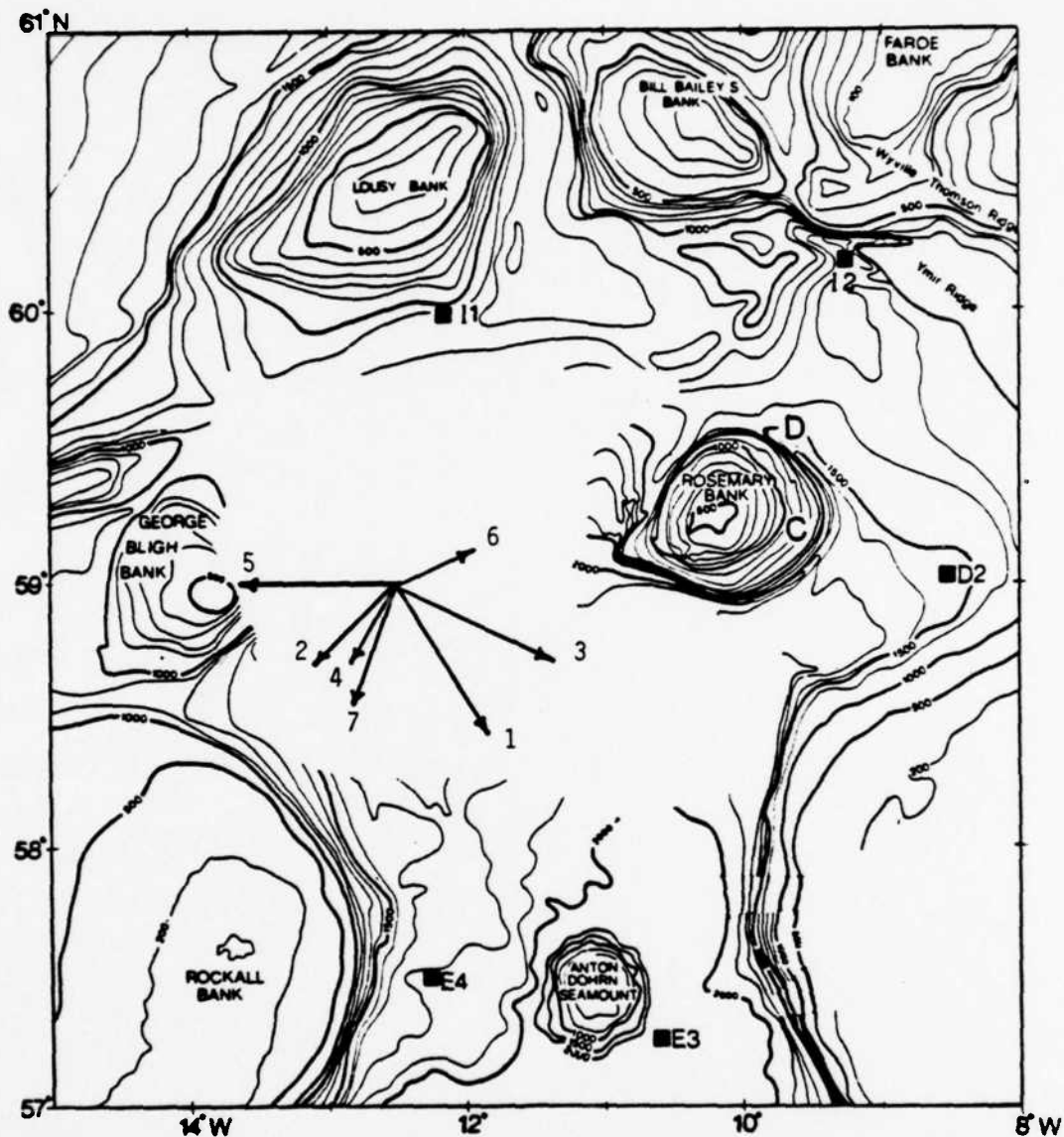


Figure 3.15. Schematic directions of internal tide packets during seven periods of intense baroclinic tide activity. The arrows point toward probable sources of the internal tides, and their lengths are roughly proportional to the shear magnitude. The directions of propagation are listed in Table 3.1, but are indeterminate to within 180° .

during Periods 2, 4, and 7, the Rockall Bank was the most likely source, in agreement with the argument of Levine et al. (1982) that this feature is an effective generator of internal tides.

Section 4

SHEAR STATISTICS

4.1 FILTERING PROCESS

As discussed in Section 3.2, there is considerable mesoscale activity in the shear measurements. In order to eliminate the low-frequency mesoscale portion of the signal, but to retain the higher-frequency internal wave component, it is appropriate to apply a high-pass filter to the time series. This filter is in addition to the low-pass filter operation described in Section 2.1. A symmetric weighting function was convolved with each current meter instrument record. The resultant filtering process had a stop band in the frequency range 0 - 0.04 cph, and a transition band in the range 0.04 - 0.08 cph. Therefore most of the variance in the internal wave band, including the semidiurnal frequency (0.0805 cph), was retained in the filtered measurements.

4.2 $S^2 - N^2$ CORRELATIONS

In this section we present correlations between mean-square Vaisala frequency $\overline{N^2}$ and mean-square shear $\overline{S^2}$, over five different vertical separations Δz . There are two purposes. First, we establish the fact that there is significant correlation between $\overline{N^2}$ and $\overline{S^2}$, and that the correlation improves with increasing Δz . Second, we can then compute the regression coefficient b , as a function of Δz . The results may then be compared against the statistical shear model, derived in Appendix B.

We began by applying the filtering process described in Section 4.1 to all of the current meter records.

Then we split the records into two non-contiguous periods; Period 1 was during the first third of the time series 31 July to 9 August and Period 2 was during the last third 23 August to 6 September (see Figure 3.8). As explained in Section 2, there was fairly continuous CTD survey coverage during these periods, but during the middle third there was no coverage. As it turns out, Periods 1 and 2 were characterized by strong and weak mesoscale activity, respectively. Thus we have conveniently managed to separate the time series into two quite different regimes.

Figures 4.1 - 4.5 show observed values of $\overline{S^2}$ as functions of N^2 , for vertical separations $\Delta z = 3, 6, 12, 15,$ and 24 m. Period 1 observations are represented by triangles and Period 2 by crosses. The solid and dashed lines represent the origin-forced least-squares fits for Periods 1 and 2, respectively. Note that the slopes of the Period 1 lines are all greater than those for Period 2.

The results from a regression analysis are tabulated in Table 4.1. The values of the regression coefficients b range from 0.2 to 1.51 during Period 1, and from 0.14 to 0.86 during Period 2. The correlation coefficients range from 0.90 to 0.99. It is interesting that the correlation coefficients increase with Δz . The reason for this effect has to do with the fact that the observed mean-square velocity difference $\overline{S^2} \Delta z^2$ increases with Δz (see the last column in Table 4.1), while the noise due to instrument calibration error and mooring motion remains constant. Therefore the relative importance of noise decreases with increasing Δz . We also computed the uncertainty σ_b in the

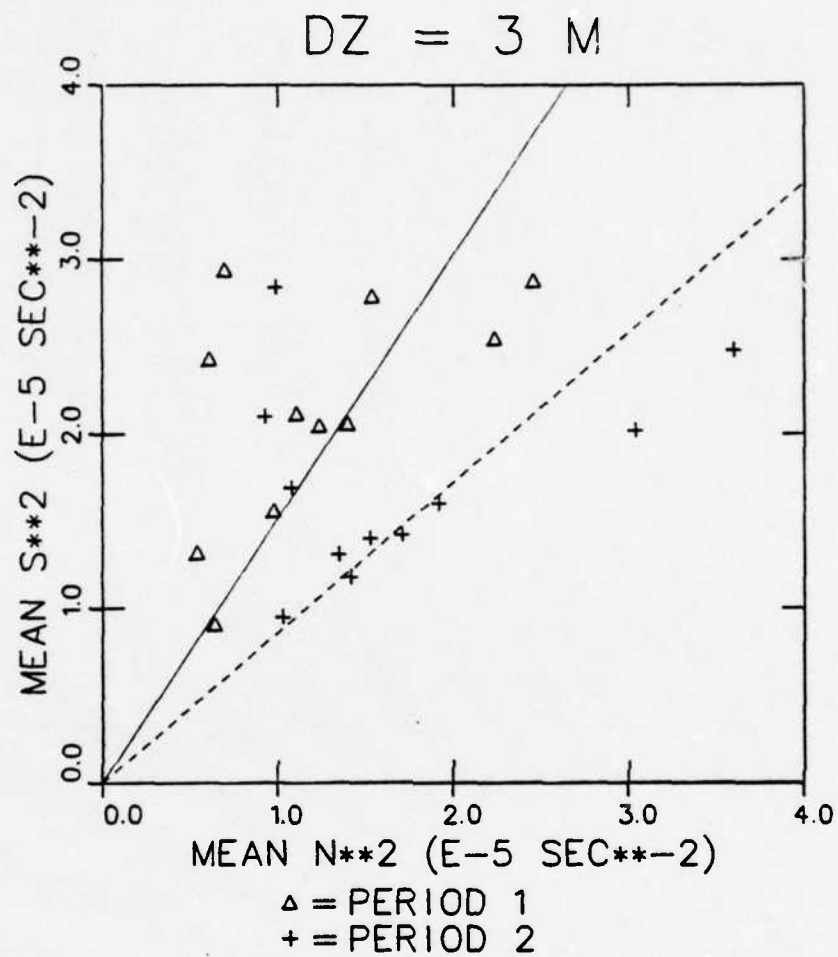


Figure 4.1. Mean-square shear across 3 m intervals vs. mean-square Vaisala frequency, during Period 1 (31 July to 9 August) and Period 2 (23 August to 6 September).

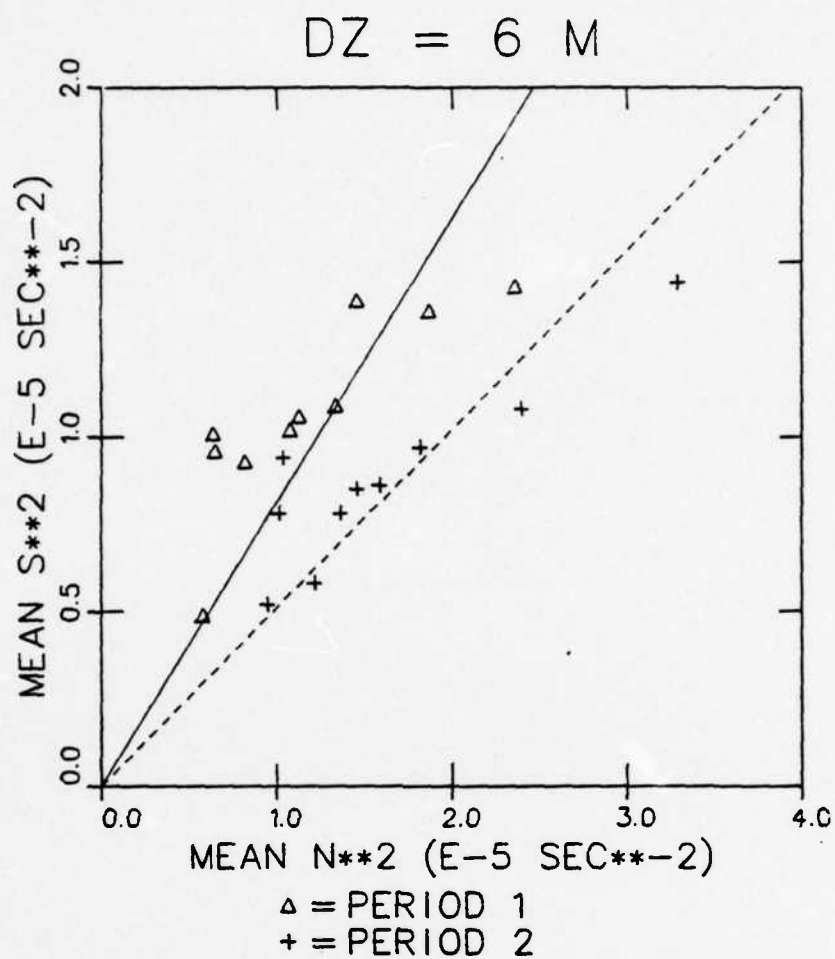


Figure 4.2. Mean-square shear across 6 m intervals vs. mean-square Vaisala frequency, during Period 1 (31 July to 9 August) and Period 2 (23 August to 6 September).

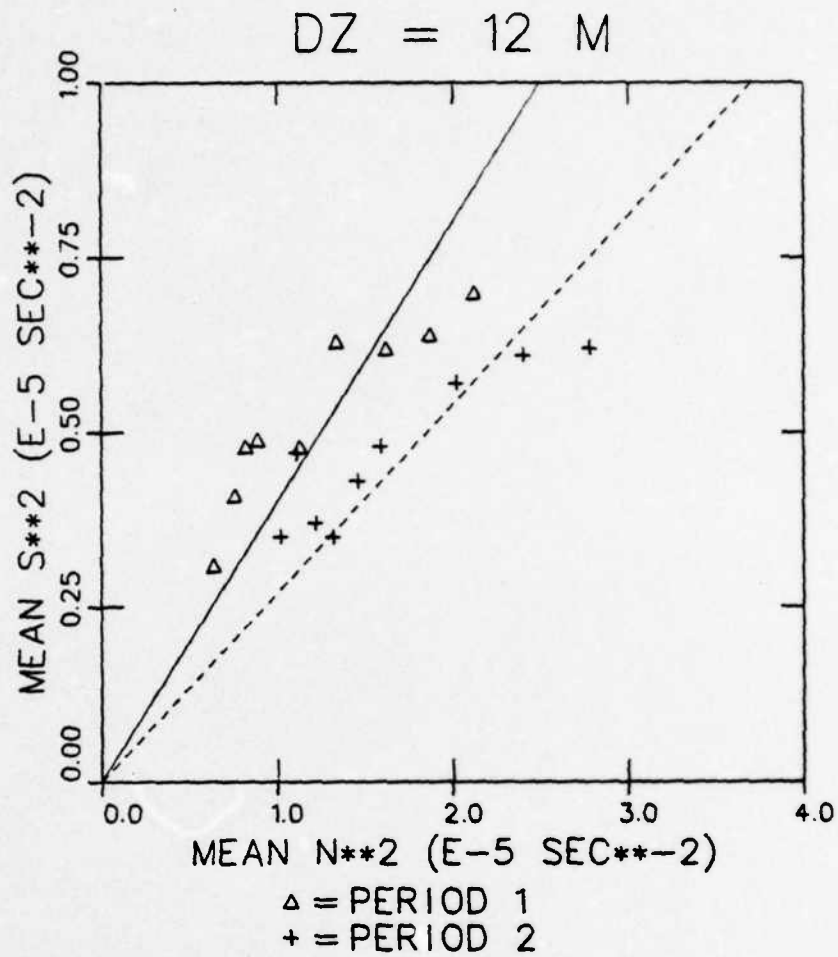


Figure 4.3. Mean-square shear across 12 m intervals vs. mean-square Vaisala frequency, during Period 1 (31 July to 9 August) and Period 2 (23 August to 6 September).

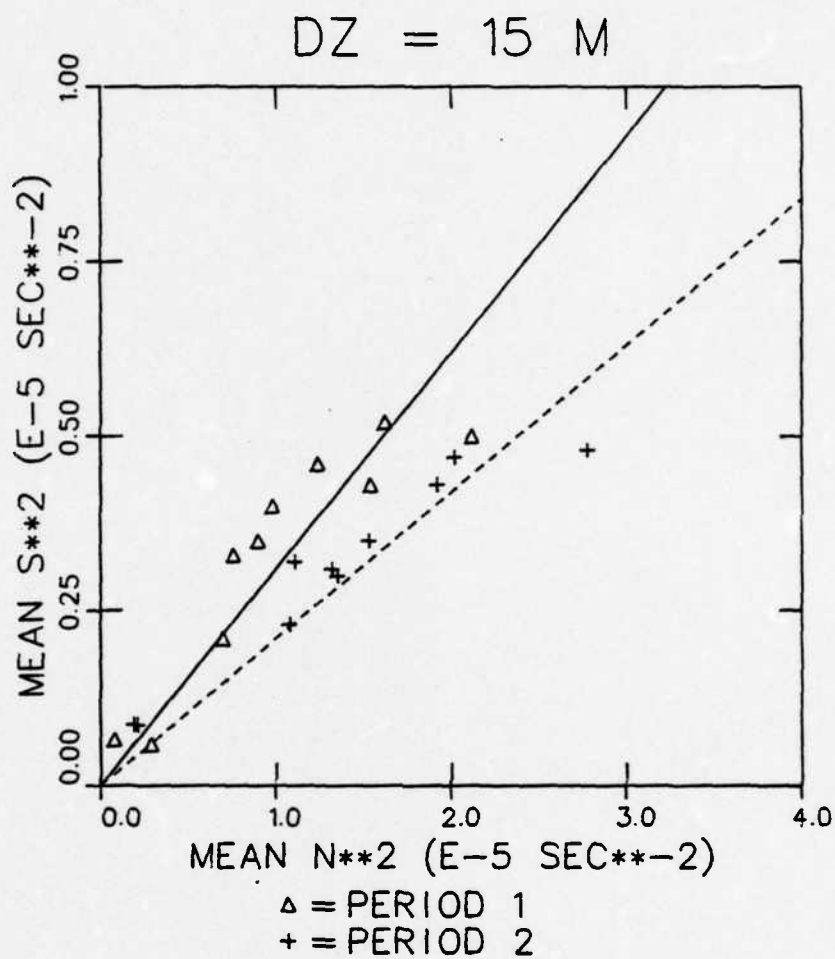


Figure 4.4. Mean-square shear across 15 m intervals vs. mean-square Vaisala frequency, during Period 1 (31 July to 9 August) and Period 2 (23 August to 6 September).

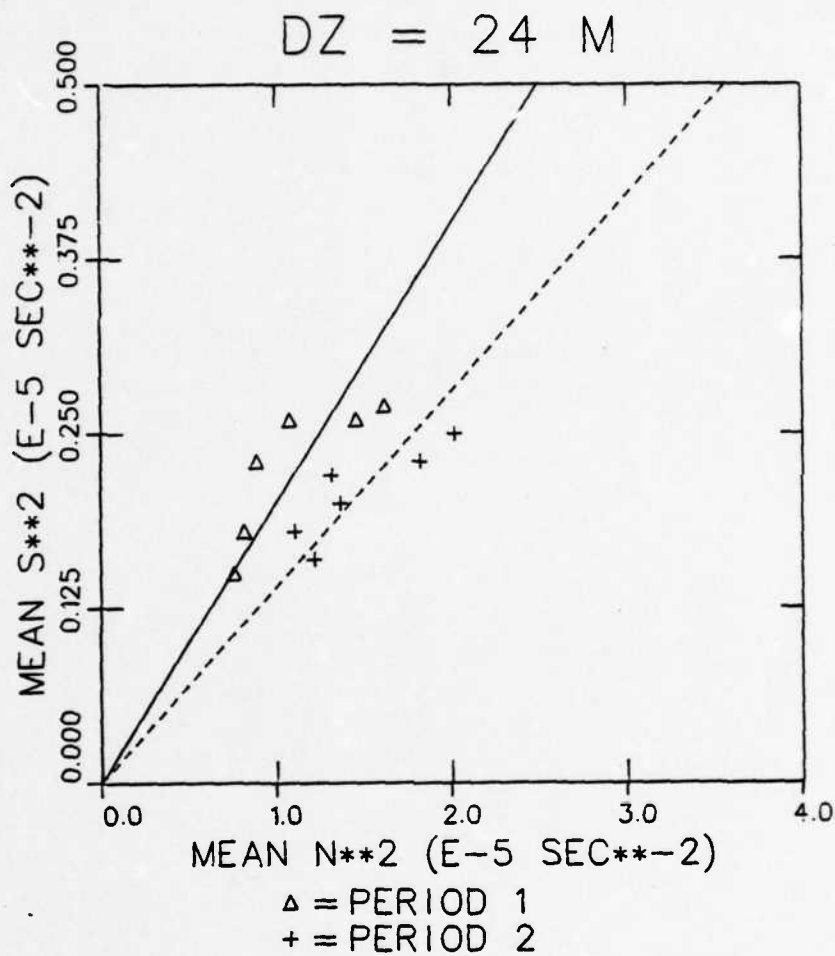


Figure 4.5. Mean-square shear across 24 m intervals vs. mean-square Vaisala frequency, during Period 1 (31 July to 9 August) and Period 2 (23 August to 6 September).

Table 4.1

LEAST-SQUARES REGRESSION COEFFICIENTS $\overline{S^2} = \overline{bN^2}$

	$\Delta z(m)$	b	r	σ_b/b	$\frac{\overline{S^2 \Delta z^2}}{\overline{2N^2/k_0}} = b \Delta z^2 k_0 / 2$
Period 1	3	1.51	0.93	0.13	4.27
	6	0.81	0.96	0.09	9.16
	12	0.40	0.98	0.07	18.10
	15	0.31	0.98	0.07	21.91
	24	0.20	0.99	0.08	36.19
Period 2	3	0.86	0.90	0.15	2.43
	6	0.50	0.98	0.07	5.65
	12	0.27	0.99	0.06	12.21
	15	0.21	0.99	0.05	14.84
	24	0.14	0.99	0.05	25.33

regression coefficient estimates. To a good approximation, $\sigma_b = 0.14b$ for $\Delta z = 3$ m, and $\sigma_b = 0.07b$ for $\Delta z = 6, 12, 15,$ and 24 m.

4.3 ANALYSIS

The last column in Table 4.1 lists the mean-square velocity difference $\overline{S^2 \Delta z^2}$, normalized by the factor $2N^2/k_0$. The values are plotted in Figure 4.6, along with the results from a similar analysis from MILE (Rubenstein, 1982, 1983). Note that for each experiment period, the normalized mean-square velocity difference increases linearly with Δz .

The solid and dashed curves represent the statistical model predictions (see Appendix B) for the variance factors $A = 1$ and 0.7 , respectively. The empirical variance factor A allows the model to adjust for regions in proximity to sources and sinks of internal waves. It is evident that the MILE and JASIN Period 2 data agree best with the factor $A = 0.7$, and the JASIN Period 1 data agree with $A = 1.0$. The implication is that shear in the internal wave frequency band was higher during Period 1 of JASIN, when the local mesoscale activity was substantial.

It should be emphasized again that the current records were low pass filtered prior to the computations of the mean-square shear. Only shear in the internal wave frequency band (0.08 - 2.5 cph) was retained. Therefore, the enhanced level of shear during Phase I of JASIN, shown in Figure 4.6, was not directly due to the mesoscale activity. Instead, the variable mesoscale field was probably responsible for significant changes in the propagation, and perhaps also in the generation, of near inertial wave-induced shear.

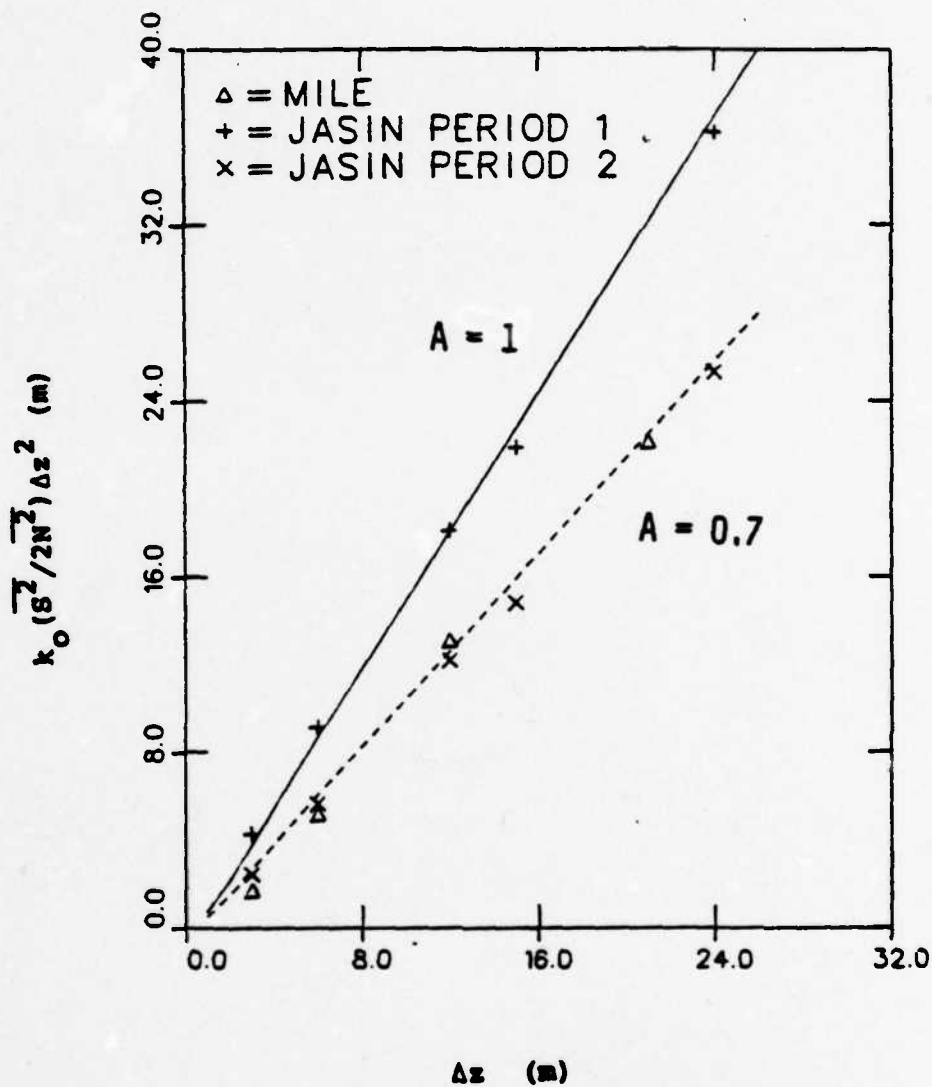


Figure 4.6. Mean square velocity difference vs vertical separation interval, Δz . The JASIN Period 1 data fit the model with $A=1$, and the JASIN Period 2 and MILE data are best with $A=0.7$.

Section 5

CONCLUSIONS

During the JASIN 1978 experiment, the semidiurnal component of shear exhibited seven periods of particular intensity. These periods typically lasted one or two days each. They can be identified with strong internal tides, as revealed by records of temperature oscillations. Therefore, it seems appropriate to analyze the semidiurnal shear as a deterministic signal.

During the seven periods of intense semidiurnal shear, the eccentricity and orientation of the shear ellipse orbit were analyzed. The eccentricity was computed in terms of the minor-to-major axis ratio, whose peak values during the intense periods ranged from 0.80 to 0.98. This range is consistent with the theoretical value $f/\omega = 0.89$, for a coherent internal wave of frequency ω , and inertial frequency f . If the semidiurnal shear is associated with a single, coherent source of internal tides, then the orientation of the shear ellipse indicates the direction of propagation. Hence the source of the internal waves can be identified (but only to within 180°). The generation of an internal tide requires the interaction of the barotropic tide with a steeply sloped bottom feature. Therefore, in some cases the 180° ambiguity could be removed, in favor of a nearby bottom feature. In certain cases however, the ambiguity could not be removed, because the shear ellipse was not directly aligned in the direction of a nearby bottom feature. It is possible that during those periods, internal wave packets

were arriving simultaneously from two or more directions, preventing a correct determination of the direction of either source.

The statistical model of shear predicts that mean-square velocity difference should be approximately linearly proportional to the vertical differencing interval Δz , and to the mean-square Vaisala frequency $\overline{N^2}$. For scales greater than two meters the relation is approximately

$$\overline{\Delta u^2} + \overline{\Delta v^2} \equiv \overline{S^2} \Delta z^2 = \frac{A\pi}{k_0} \overline{N^2} \Delta z, \quad (5.1)$$

where k_0 is the fall-off wavenumber of the shear spectrum. Results from MILE and JASIN substantiate (5.1) over a large range of $\overline{N^2}$.

The variance factor A might depend on the mesoscale eddy field. During MILE and JASIN Period 2, A was 0.7. During JASIN Period 1 and in the Sargasso Sea--both relatively eddy-rich environments-- A was 1.0. The geostrophic current associated with mesoscale eddies profoundly affects the propagation of low frequency internal waves. During JASIN, the internal tide would have been especially affected. Exactly how the factor A depends on the mesoscale environment is not yet understood. Additional theoretical studies of internal-wave/baroclinic-current interactions, closely coupled with analyses of existing shear data are recommended.

APPENDIX A

COMPLEX DEMODULATION

The technique of complex demodulation was used to demodulate a vector time series at the semidiurnal tidal frequency $f_0 = 1/12.4$ cph. Kundu (1976) and Pollard (1980) used a similar technique to separate out the inertial frequency component from other frequency components in vector current time series.

In descriptive terms, complex demodulation can be understood as follows. Consider a vector time series, with a significant tidal component that rotates clockwise with frequency f_0 . The vector time series $(u(t), v(t))$ can be written as a complex-valued time series $U(t) = u(t) + iv(t)$. Then we multiply $U(t)$ by a unit-magnitude complex vector $\exp(2\pi if_0 t)$. This operation is equivalent to a transformation to a new coordinate system, which rotates clockwise with frequency f_0 . In this coordinate system, the amplitude of the steady-state signal corresponds to the magnitude of the tide. Therefore, it is appropriate to apply an averaging integral, and thereby isolate the steady-state amplitude. Unfortunately, a simple integral (equation A.1, below) tends to include frequency components that are far removed from the frequency of interest, f_0 . A more sophisticated approach is to incorporate a specially designed weighting function, called a filtering lag function $W_L(t)$, inside the integral. This method helps to isolate better the desired frequency component.

Let $U(t) = u + iv$ be the original vector time series. The most simple formulation of the demodulated series is

$$D(t) = \frac{1}{T} \int_{t-T/2}^{t+T/2} U(\tau) e^{2\pi i f_0 \tau} d\tau, \quad (A.1)$$

where T is the averaging time. It is obvious that (A.1) is simply the convolution of a rectangular lag function

$$W_R(t) = \begin{cases} 1/T & |t| < T/2 \\ 0 & |t| > T/2 \end{cases} \quad (A.2)$$

with the integrand of (A.1);

$$D(t) = \int_{-\infty}^{\infty} W_R(\tau) U(t-\tau) e^{2\pi i f_0 (t-\tau)} d\tau. \quad (A.3)$$

By the convolution theorem, the Fourier transform $\hat{D}(f)$ (indicated by the caret) of $D(t)$ is given by

$$\hat{D}(f) = \hat{W}_R(f) \hat{U}(f+f_0). \quad (A.4)$$

However, the rectangular spectral window function is

$$\hat{W}_R(f) = \frac{\sin \pi f T}{\pi f T}. \quad (A.5)$$

This function has very large side lobes, which slowly decay as f^{-1} . In order to suppress these side lobes a special low-pass filtering lag function $W_L(t)$ can be applied. Its frequency response $\hat{W}_L(f)$ is shown in Figure A.1. It is designed to have a cut-off frequency $f_c = 0.016$ cph, as

RESPONSE

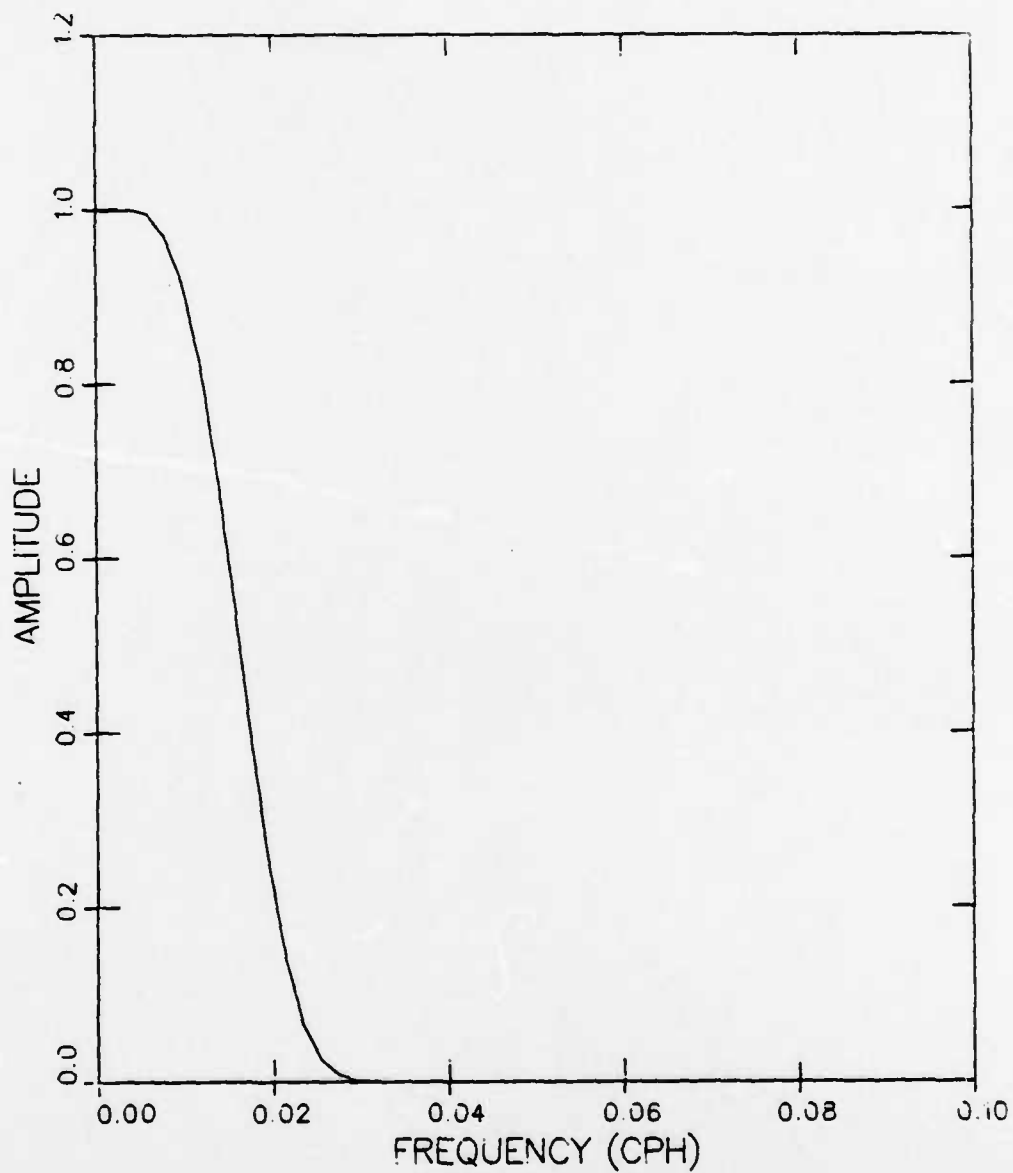


Figure A.1. Amplitude of the frequency response function $\hat{w}_L(f)$. The amplitude is 0.5 at the cut-off frequency $f_c = 0.016$ cph.

shown in the figure. Note that the side lobes (the single-sided spectrum is shown here) are too small to be noticeable on this linear plot.

The complex demodulation technique was performed using (A.3), but with W_L in place of W_R . The demodulated signal $D(t)$ was decomposed into an amplitude and a phase,

$$D(t) = |D(t)| e^{i\phi(t)}, \quad (A.6)$$

where

$$\phi = \arctan (-\text{Im}D/\text{Re}D), \quad (A.7)$$

and

$$|D| = [(\text{Re}D)^2 + (\text{Im}D)^2]^{1/2}. \quad (A.8)$$

The amplitude $|D|$ gives the amplitude of the signal $U(t)$ within the bandwidth $f_0 - f_c < f < f_0 + f_c$. With $f_0 = 1/12.4$ cph and $f_c = 0.016$ cph, the range of periods is 15.47 hr to 10.35 hr. Thus the inertial period at the latitude 59° , 14.0 hr, is included within this range. The time series $\phi(t)$ gives the phase of the signal $U(t)$ with respect to the clockwise rotating unit vector $e^{-2\pi i f_0 t}$. If $\phi(t)$ decreases (increases) with time, then $U(t)$ --within the bandpass interval $f_0 - f_c < f < f_0 + f_c$ --rotates clockwise faster (slower) than a pure tidal oscillation with frequency f_0 .

APPENDIX B STATISTICAL MODEL OF MEAN-SQUARE SHEAR

In this section we present a statistical model first derived by Rubenstein, Newman, and Grabowski (1983). The model predicts how measurements of mean-square shear vary with the vertical separation Δz between current meters. We begin by representing the complex valued velocity field $U(z) = u(z) + iv(z)$ as an inverse Fourier integral

$$U(z) = \frac{1}{2\pi} \int_{-\infty}^{\infty} U(k) e^{ikz} dk , \quad (B.1)$$

where k is the vertical wavenumber. The spectral density function is

$$P_U(k) = \langle U(k)U^*(k) \rangle , \quad (B.2)$$

where the brackets denote an ensemble average.

Suppose we were to sample $U(z)$ at discrete intervals and estimate the shear $S(z, \Delta z)$ by performing a first differencing operation;

$$S(z, \Delta z) = \frac{U(z + \Delta z) - U(z)}{\Delta z} . \quad (B.3)$$

Taking the Fourier transform of (B.3), we get

$$S(k, \Delta z) = \frac{-2iU(k)}{\Delta z} \exp(-ik\Delta z/2) \sin(k\Delta z/2) . \quad (B.4)$$

Therefore, the spectral density $P_S(k, \Delta z)$ of shear over a finite interval Δz is

$$P_S(k, \Delta z) = 4P_U(k) \left(\frac{\sin(k\Delta z/2)}{\Delta z} \right)^2 . \quad (B.5)$$

In the limit as Δz goes to zero,

$$P_S(k) = \lim_{\Delta z \rightarrow 0} P_S(k, \Delta z) = k^2 P_U(k) . \quad (B.6)$$

In Figure B.1 we illustrate a shear spectrum model $P_S(k)$, which is an idealized form of the composite spectrum published by Gargett et al. (1981). The form of this model is

$$P_S(k) = \begin{cases} AN^2/k_0 & k < k_0 \\ AN^2/k & k_0 < k < k_b , \end{cases} \quad (B.7)$$

where N is the local Vaisala frequency, expressed in rad s^{-1} , k_0 is taken as 0.628 rad m^{-1} , and the buoyancy wavenumber, k_b , is taken as 6.28 rad m^{-1} ($k_0 = 0.1 \text{ cpm}$, $k_b = 1 \text{ cpm}$). If the total observed variance is equal to that observed by Gargett et al. (1981), then the value of the variance factor is $A=1$. The energy level of internal waves is commonly observed to vary by a factor of ± 2 . Therefore, the variance factor A is included in (B.7) in order to adjust for regions which are in proximity to sources and sinks of internal waves.

We do not include contributions from the high wavenumber turbulence dissipation range in this model. We substitute (B.6) and (B.7) into (B.5) and integrate over wavenumber to obtain the expected value of mean-square shear;

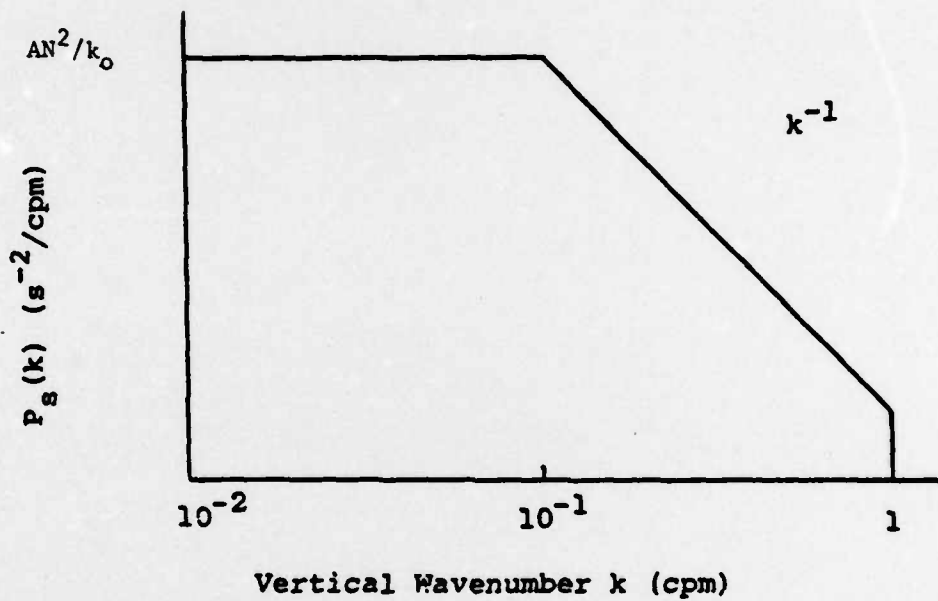


Figure B.1.

Idealized Shear Spectrum after Gargett et al. (1981)

Roll-off Wavenumber $k_0 = 0.1 \text{ cpm}$

Buoyancy wavenumber $k_b = 1 \text{ cpm}$

$$\begin{aligned} \langle |S(z, \Delta z)|^2 \rangle &= A(N^2/k_0) \int_0^{k_0} \left[\frac{\sin(k\Delta z/2)}{k\Delta z/2} \right]^2 dk \\ &+ AN^2 \int_{k_0}^{k_b} k^{-1} \left[\frac{\sin(k\Delta z/2)}{k\Delta z/2} \right]^2 dk . \end{aligned} \quad (B.8)$$

Writing $y = k\Delta z/2$, $y_0 = k_0\Delta z/2$, and $y_b = k_b\Delta z/2$, equation (B.8) becomes

$$\langle |S(z, \Delta z)|^2 \rangle = \frac{2AN^2}{\Delta z k_0} \int_0^{y_0} \frac{\sin^2 y}{y^2} dy + AN^2 \int_{y_0}^{y_b} \frac{\sin^2 y}{y^3} dy . \quad (B.9)$$

The first integral I_1 in (B.9) is

$$I_1 = \frac{\cos 2y_0 - 1}{2y_0} + \text{Si}(2y_0) , \quad (B.10)$$

and the second integral I_2 is

$$\begin{aligned} I_2 = \frac{1}{4} [y_b^{-2}(\cos 2y_b - 1) - 2y_b^{-2} \sin 2y_b - y_0^{-2}(\cos 2y_0 - 1) \\ + 2y_0^{-1} \sin 2y_0] - \text{Ci}(2y_0) + \text{Ci}(2y_b) , \end{aligned} \quad (B.11)$$

where

$$\text{Si}(x) = \int_0^x t^{-1} \sin t dt$$

and

$$\text{Ci}(x) = - \int_x^\infty t^{-1} \cos t dt \quad (B.12)$$

are the sine and cosine integrals. A model prediction of normalized mean-square velocity difference

$$\frac{\langle S|z, \Delta z|^2 \rangle \Delta z^2 k_0}{2N^2} = A \Delta z (I_1 + k_0 \Delta z I_2 / 2) , \quad (B.13)$$

and the separate contributions from I_1 and I_2 are plotted in Figure B.2. The contributions from I_1 and I_2 are comparable for $k_0 \Delta z \approx 1$. For large Δz , the contribution from I_2 is approximately uniform; the contribution from I_1 dominates, and the mean-square velocity differences become asymptotically proportional to Δz . Since in the limit as $y_0 \rightarrow \infty$, $Si(2y_0) \rightarrow \pi/2$, we note that a useful approximation for (B.13) is

$$\frac{\langle S|z, \Delta z|^2 \rangle \Delta z^2 k_0}{2N^2} \approx \frac{A\pi}{2} \Delta z . \quad (B.14)$$

The model is quite insensitive to the value to k_0 . Even though the value is ill-defined within the range $\pi/10 < k_0 < 2\pi/5$ rad m^{-1} , the mean-square velocity difference over large Δz is predicted within a well-defined range. This narrow range is outlined by the lower and upper dashed curves in Figure B.3.

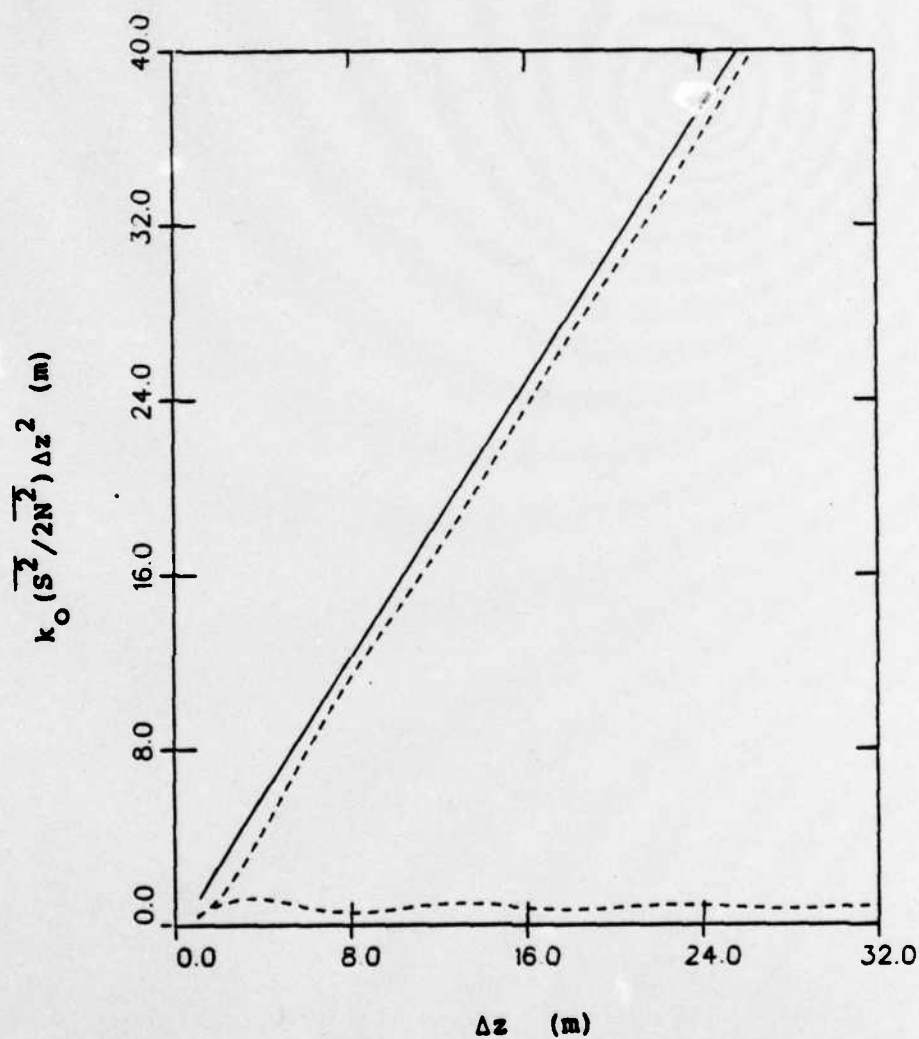


Figure B.2. Model prediction of mean-square velocity difference, from Equation (B.13). Parameter values are $k_0 = 0.1$ cpm, $k_b = 1$ cpm, and $A = 1$. The two dashed curves indicate the separate contributions due to I_1 and I_2 , and the solid curve is the sum total.

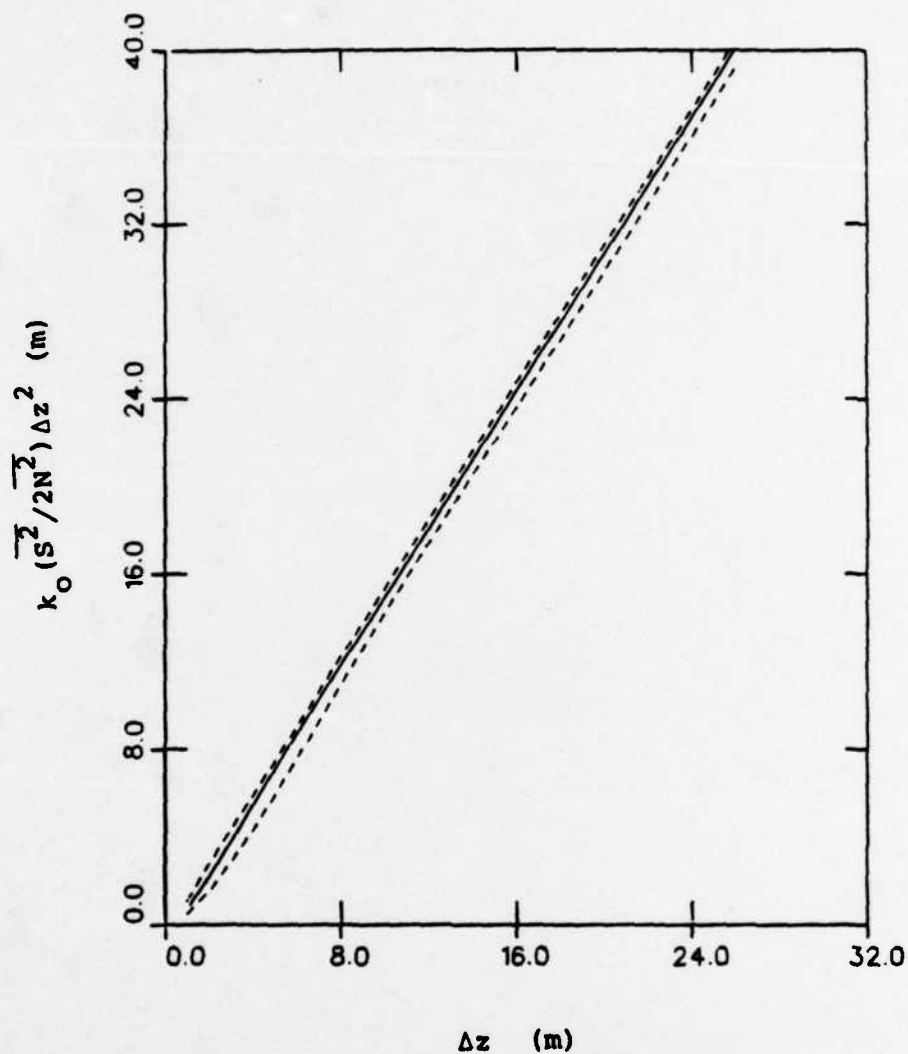


Figure B.3. Model prediction for mean-square velocity difference over vertical differencing interval Δz . The fall-off wavenumber values are $k_0 = 0.1$ cpm for the solid curve, and $k_0 = 0.2$ and 0.05 cpm for the upper and lower dashed curves, respectively. The narrow range between the dashed curves indicates the model's insensitivity to the value of k_0 .

REFERENCES

- Ellett, D. J., P. Kruseman, G. J. Pragsma, R. T. Pollard, H. M. Van Aken, A. Edwards, H. D. Dooley, and W. J. Gould, 1983: Water masses and mesoscale circulation of North Rockall Trough waters during JASIN 1978. Phil. Trans. R. Soc. London A., 308, 231-252.
- Kundu, P. K., 1976: An analysis of inertial oscillations observed near Oregon coast. J. Phys. Oceanogr., 6, 879-893.
- Levine, M. D., C. A. Paulson, M. G. Briscoe, R. A. Weller, and H. Peters, 1983: Internal waves in JASIN. Phil. Trans. R. Soc. London A., 308, 389-405.
- Mamayev, O. I., 1975: Temperature-Salinity Analysis of World Ocean Waters. American Elsevier Publishing Company, Inc., New York.
- McCullough, J. R., 1975: Vector-averaging current meter speed calibration and recording technique, WHOI-75-44, Woods Hole Oceanographic Institution.
- Pollard, R. T., 1980: Properties of near-surface inertial oscillations. J. Phys. Oceanogr., 10, 385-398.
- Pollard, R. T., 1983: Mesoscale (50-100 km) circulations revealed by inverse and classical analysis of the JASIN hydrographic data. J. Phys. Oceanogr., 13, 377-394.
- Pollard, R. T., and R. C. Millard, Jr., 1969: Comparisons between observed and simulated wind-generated inertial oscillations. Deep-Sea Research, 17, 813-821.
- Prangma, G. J., T. H. Guymer, P. Kruseman, R. T. Pollard, and R. A. Weller, 1983: Development of the temperature and salinity structure of the upper ocean over two months in an area 150 x 150 km. Phil. Trans. R. Soc. London A. 308, 311-325.
- Regal, R., and C. Wunsch, 1973: M_2 tidal currents in the Western North Atlantic. Deep-Sea Research, 20, 493-502.
- Rubenstein, D. M., and F. C. Newman, 1982a: Statistical analysis of upper ocean time series of vertical shear, SAI-83-751-WA, Science Applications, Inc., 65 pp.

REFERENCES (cont.)

Rubenstein, D. M., and F. C. Newman, 1982b: Analysis of shear from ocean current meters, SAI-82-687-WA, Science Applications, Inc., 92 pp.

Rubenstein, D. M., F. C. Newman, and W. Grabowski, 1983: A statistical model of vertical shear from moored current meters. J. Phys. Oceanogr., 13, 966-971.

Tarbell, S., M. G. Briscoe, and R. A. Weller, 1979: A compilation of moored current meter and recorder data. Volume XVIII (JASIN 1978, Moorings 651-653), WHOI-79-65, Woods Hole Oceanographic Institution, 233 pp.

Weller, R. A., 1982: The relation of near-inertial motions observed in the mixed layer during the JASIN (1978) experiment to the local wind stress and to the quasi-geostrophic flow field. J. Phys. Oceanogr., 12, 1122-1136.

DATE
FILME